PROCEEDINGS OF THE WORKSHOP ON 17 – 18 JUNE 2009, DELFT, THE NETHERLANDS

Computational Modeling on Concrete, Masonry and Fiber-reinforced Composites

Edited by:
Max Hendriks
Sarah Billington

Delft University of Technology

ISBN: 978-94-90284-03-9

Printed in The Netherlands

Table of Contents

Preface

This booklet comprises the extended abstracts to be presented at the Ma(gni)FiCo workshop held in Delft, The Netherlands, on 17-18 June 2009. The spirit of this workshop is to have a small gathering with ample time for lively conversation and interaction among the student and faculty researchers.

As a partial acronym, Ma(gni)FiCo stands for a Computational Modeling Workshop on Masonry, Fiber-reinforced Composites and Concrete. The theme of the workshop is computational modeling with two primary focus areas – masonry and fiber-reinforced composites (cement-based and polymeric). Several research areas "bridge" these topics, such as the modeling and analysis techniques being used to evaluate these and other brittle materials. Furthermore, several participants are researching structural designs that combine masonry and composites.

We would like to express our sincere gratitude to all participants for accepting our invitation to participate in this workshop and for taking the time to travel to Delft. We would also like to thank Ms. Marjon van der Perk for helping organize this workshop and Ms. Widyani Sutjiadi for assembling our workshop proceedings.

Max Hendriks
Sarah Billington

Delft, June 2009

Structural jacketing of brick masonry columns: a comparison among different solutions

B. Belletti
DICATeA, University of Parma, Italy and Faculty of Architecture, TUDelft, The Netherlands

E. Coïsson
DICATeA, University of Parma, Italy

Keywords: restoration, brick masonry, structural jacketing, CFRP sheets, structural repointing, steel belts.

INTRODUCTION

The use of fiber-reinforced composites to strengthen historical masonries often encounters problems of architectural compatibility, particularly when the masonry is unplastered. In these cases the insertion of visible fiber sheets isn't usually acceptable; on the contrary, the use of steel elements is easier, as iron elements have been traditionally applied since several centuries to retrofit ancient masonry structures.

The authors believe that it is not possible to study the applications of fibers on historical buildings without considering also the aesthetic aspects. Therefore, facing a real case of strengthening needed by some columns in an Italian castle, different structural solutions, with different aesthetic impacts, have been inspected:

a) complete covering of the columns with CFRCM;
b) discontinuous stripes of CFRCM;
c) discontinuous stripes of CFRP;
d) structural repointing of the joints with thin stripes of CFRP;
e) steel belts.

Figure 1: the Rocca di Fontanellato (left) and its “loggia” (right), whose columns need strenghtening.

THE REAL CASE: THE ROCCA DI FONTANELLATO

The real case to which these solutions should be applied, is the inner “loggia” of the XV century Rocca di Fontanellato (Fig. 1), whose bricks columns, capitals and arches show a widespread crack pattern. Indeed, the mean stresses at the base of the columns are quite high: 1.74 MPa considering only the dead loads, raising to 1.94 MPa considering also the live loads. Moreover,

the connection of the iron ties to the wall above the capitals has shown inefficient, as demonstrated also with on site dynamic tests, causing eccentric loads on the columns.

The fact that columns, capitals and arches are all unplastered makes it more difficult to find an appropriate solution from the aesthetic point of view, as required by the local cultural heritage protection offices.

THE EXPERIMENTAL TESTS

Two sets of laboratory tests have been performed in order to inspect the structural behavior of the different solutions considered. Overall, 30 specimens, made with new semi-circular bricks and lime mortar, were tested under compression, following the prescriptions of UNI EN 1052-1: 2001. The specimens of the first set were 54 cm high and 19.5 cm in diameter; the specimens of the second set were 66 cm high and 23 cm in diameter.

The mechanical characteristics of the materials composing the specimens (bricks and mortar) were also tested in laboratory. The mortar was tested following the UNI EN 1015-11, obtaining a mean compression strength of 10,93 MPa for the first set and 9.34 MPa for the second set (M10 type mortar). The bricks instead showed a greater difference between the two sets: the tests carried out following the UNI EN 772-1:2002 showed a mean compression strength of 7.6 MPa for the first set and 27.5 MPa for the second set. For each strengthening solution, 3 specimen were then tested, adopting the labels reported in Table 1.

First set – type of specimen	Label
Unreinforced	NR1
Complete covering with CFRCM	RT1
Discontinuous stripes with CFRCM	RS1
Structural repointing with CFRP	RG1
Steel belt	CM1
Second set – type of specimen	
Unreinforced	NR2
Complete covering with CFRCM	RT2
Discontinuous stripes with CFRP	RS2
Structural repointing with CFRP	RGT2
Structural repointing with CFRP every second joint	RG2

Table 1: strengthening solutions.

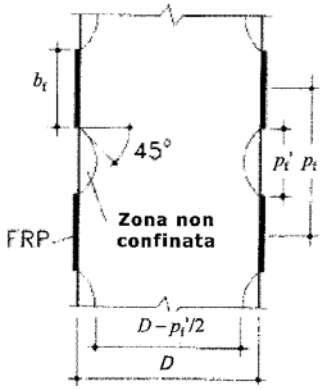

Figure 2: parameters for the evaluation of confinement effects by CNR DT – 200.

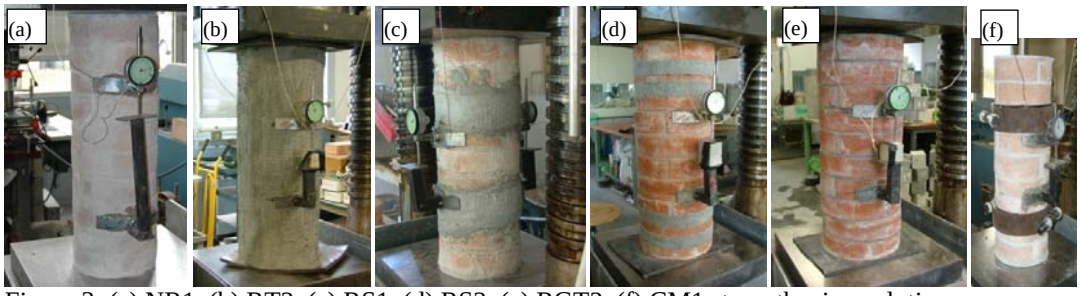

Figure 3: (a) NR1, (b) RT2, (c) RS1, (d) RS2, (e) RGT2, (f) CM1 strengthening solutions.

For the CFRCM reinforced specimens, the Ruredil X MESH C10 was applied. For the CFRP reinforced specimen, the SikaWarp-300(VP) / Sikadur-330 was applied. The steel belts were 219.1 mm in diameter and 10 mm thick, applied at 240 mm of spacing. Only for the steel belts a pre-stress could be applied, with a graded key regulated at 30 Nm. The second set of specimens was realized by an expert restorer: in Fig. 4 all the steps needed for the strengthening with repointing technique are reported.

Figure 4: steps for the strengthening with repointing technique (step a: cleaning, step b: protection of brick elements, step c: cutting of carbon fibers, step d: application of epoxy resin and layers of fibers, step e: application of quartz grains, step f: application of mortar).

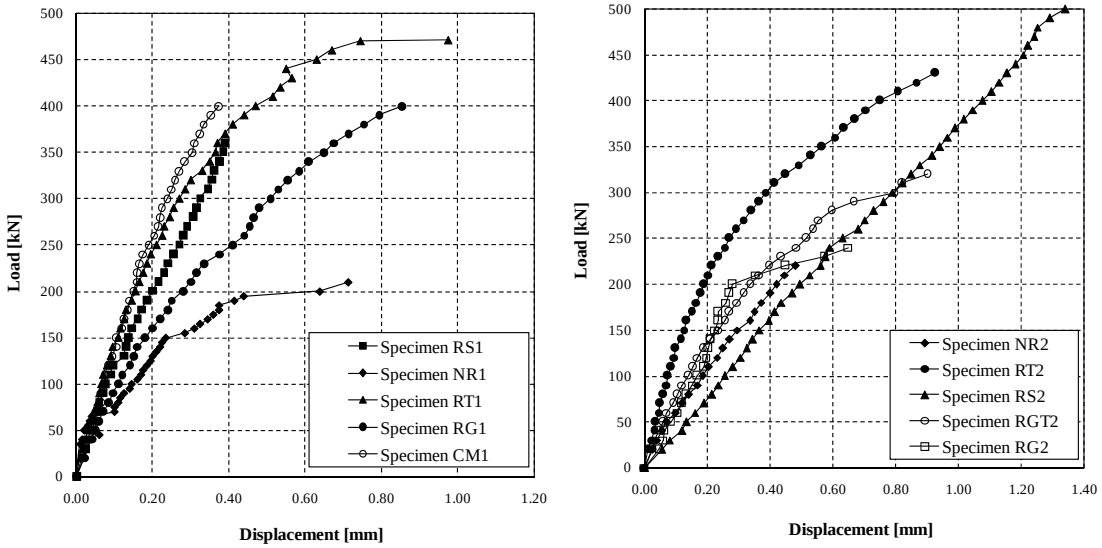

Figure 5: the load-displacement curves of the different strengthening solutions: first set on the left, second set on the right.

Figure 5 shows the load-displacement curves for the two sets of tests. The graphs report the mean values for each group of 3 specimen with the same reinforcement. Easy to predict, the reinforcement with complete covering in CFRCM shows good structural behavior, both in terms of ultimate load and of ductility. Nevertheless, this solution is also the least acceptable as far as the principles of restoration are concerned, as it conceals the original material to the sight.
The discontinuous CFRP specimens show higher strengths with respect to CFRCM specimens. The steel belt shows the stiffest behavior, as it is the only solution which allowed a pre-stressing to be applied. The structural repointing with CFRP is with no doubt the best solution from the aesthetic point of view and also shows a ductile behavior, increasing the strength of about 50% with respect to the unreinforced specimens, but it needs to be carried out on all the joints, as the application on each second joint showed much worse results. Figure 6 shows the failure mode of the tested specimens.

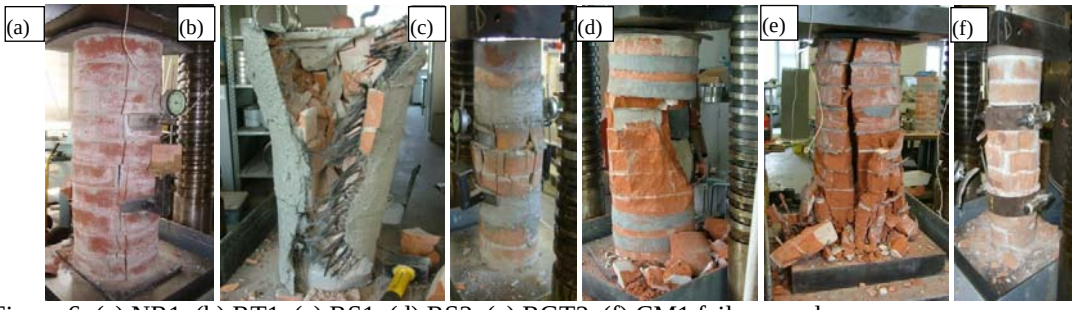

Figure 6: (a) NR1, (b) RT1, (c) RS1, (d) RS2, (e) RGT2, (f) CM1 failure modes.

The experimental compressive strengths obtained with the analyzed strengthening solutions have been compared with the values calculated following the Italian CNR-DT 200/2004: Table 2 reports these comparisons and all the data needed for the calculation of confined masonry compressive strength following CNR-DT 200/2004 (see Fig. 2).

Strengthening solution	**RT1**	**RS1**	**RG1**	**RT2**	**RS2**	**RGT2**	**RG2**
Ultimate strain ε_{fu}	0.018				0.015		
Young modulus E_f [GPa]	240						
Thickness t_f [mm]	0.047				0.177		
Number of layers	1				2		
Height of stripes b_f [mm]	-	90	15	-	125	5	5
Spacing of stripes p_f [mm]	-	240	60	-	360	65	185
Distance between stripes p'_f [mm]	-	180	45	-	235	60	180
Mean unconfined masonry strength [MPa]	8.50			5.05			
Masonry weight g_m [kg/m^3]	1600			1770			
Diameter of masonry coloumn [mm]	195			230			
Diameter of confined coloumn [mm]	205	205	195	240	230	230	230
Confined strength by Italian CNR DT-200 [MPa]	11.51	8.83	9.15	7.92	6.68	6.19	5.25
Experimental strength [MPa]	14.95	12.16	13.39	9.55	11.87	7.38	6.58

Table 2: Comparison between experimental and numerical results.

CONCLUSIONS: WHY TO PERFORM FINITE ELEMENT ANALYSES?

The choice of a strengthening technique to be applied on historical buildings must be guided not only by structural achievements, but also by aesthetic considerations. For this reason, several solutions have been tested in laboratory to find the best intervention on a real case of ancient columns strengthening. The laboratory tests have allowed to identify a good compromise between aesthetic and structural needs: the structural repointing with CFRP on all the mortar joints. For specific parts of the “loggia”, where large cracks are already present, some local applications of larger portions of CFRP can be advisable, as a higher increase in strength can be obtained, although the aesthetic impact is a little higher. All these conclusions rise from the results of tests laboratory on small, un-loaded and un-cracked specimens. How much the effective increase of compressive strengths is when these strengthening solutions are applied to existing and slender columns? The difficulties that can be encountered for the experimental set up of full scale tests on pre-loaded and/or pre-cracked specimens suggest to try to reply to this question by means of numerical simulations. The formulations proposed by CNR DT – 200/2004 consider masonry as an homogeneous material, a parametric study could investigate the role played by dimensions of columns and dimensions and strengths of constituents (mortar and unit brick) on confinement effects.

ACKNOWLEDGEMENTS

The present research was supported by the Municipality of Fontanellato. The Authors gratefully acknowledge Prof. Carlo Blasi, scientific responsible of the research contract, who provided insight and expertise that greatly assisted the study. The Authors also thank the Arché Restauri and the university laboratory technicians for the assistance in performing the experimental tests.

Nonlinear and Sequentially Linear Analysis of Tensile Strain Hardening Cement-based Composite Beams in Flexure

S.L. Billington
Stanford University,
Delft University of Technology, Faculty of Civil Engineering and Geosciences, Delft, The Netherlands

Keywords: engineered cementitious composites, flexure, nonlinear finite element analysis, smeared cracking, sequentially linear analysis, sawtooth

1 INTRODUCTION

High performance fiber reinforced cement-based composite (HPFRCC) materials have unique properties that are advantageous for many structural applications. In direct tension these materials can reach strains between 0.5% and 6% depending on material and specimen geometry. The large tensile strain capacity allows these materials to strain compatibly with steel reinforcement and achieve higher tension stiffening than traditional reinforced concrete. In compression, HPFRCC materials experience little to no spalling.

Currently there is little guidance on how to design with these materials in codes and specifications. To understand and explore more fully the potential benefits of such materials in structural applications, numerical modeling can be used. Both nonlinear finite element analysis as well as sequential linear analysis, the latter being particularly well suited for large-scale structural analyses (Rots and Invernizzi, 2004), can be used to evaluate HPFRCC material performance. In this presentation, a comparative analysis of small-scale slender beams made of engineered cementitious composites (ECC), a class of high performance fiber-reinforced cement-based composite, tested in four-point bending is made using nonlinear analysis with smeared cracking and using sequentially linear analysis. The nonlinear finite element analysis uses a total strain-based, smeared cracking model (Feenstra et al., 1998), which has proven effective in capturing global load-displacement behavior of structural-scale experiments well (e.g. Lee and Billington, 2008). The sequentially linear analysis uses a sawtooth softening crack model (Rots & Invernizzi, 2004).

2 EXPERIMENTS

The ECC for the beam experiments uses Type I/II Portland Cement, Class F fly ash, F110 Silica Sand, and water at the following weight ratios: 1:1.2:0.8:0.51. A high range water-reducing (HRWR) admixture is used (0.033 by weight of cement) and the fibers are polyvinyl alcohol (PVA), 0.5 in. (12.7mm) long, have a diameter of 0.0015 in. (0.038mm), and comprise 2% by volume of the total mix. The beams were tested in 4-point bending (i.e. simply-supported with two, equally-spaced point loads) as shown in Figure 1 and displacement was measured at mid-span. All specimens were tested in a table-top testing machine designed for educational use that loaded the specimens at a constant, quasi-static displacement rate where displacement was measured under a central loading point (between the point loads shown in Figure 1).

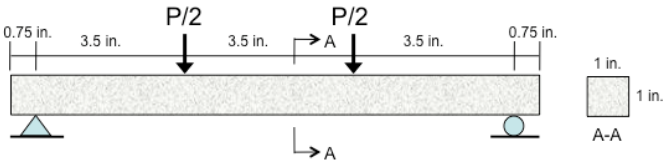

Figure 1. Beam Specimens *(1 in. = 25.4 mm)*

3 SIMULATIONS

For the nonlinear analyses, two-dimensional, 8-noded, plane stress elements of constant thickness and a 3x3 Gaussian integration scheme were used to model half of the beam with 4 elements along the height and 24 along the length. The ECC was modeled as linear elastic in compression as no softening in compression was expected nor observed in the experiments. Young's modulus was measured from an average of 4 cylinders tested in compression to be E=1,600 ksi (11,032 MPa). A total strain-based fixed crack model (Feenstra et al., 1998) was used with a tri-linear tensile stress-strain response assumed based on previous tensile tests of ECC dogbone specimens and defined by the following four stress-strain points: 1) (0,0), 2) (450 psi (3.1 MPa), 0.000281), 3) (600 psi (4.1 MPa), 0.025), and 4) (0, 0.05). A shear retention factor of 0.05 was used for the cracking and Poisson's ratio was taken as 0.15. The analyses were run in displacement control with a step size of 0.002 in. (0.05 mm) for 100 steps followed by 100 steps of 0.001 in. (0.025 mm), all applied at the loading point. The nonlinear analyses used a regular Newton-Raphson iteration scheme, including line estimation, with a maximum number of iterations of 30. Both a displacement and force tolerance of 1% were used for the convergence criteria.

For the sequential linear analyses, the same finite element model for the nonlinear analysis for half of the beam was used as described above, with the exception of using a 2x2 integration scheme rather than 3x3 in the elements. The ECC was modeled as linear elastic in compression as no softening in compression was expected nor observed in the experiments. Young's modulus was measured from an average of 4 cylinders tested in compression to be E=1,600 ksi (11,032 MPa). In tension, the same multi-linear tensile stress-strain curve from the nonlinear analysis was adopted for the baseline curve. To preserve fracture energy dissipation, a sawtooth model using an upper and lower bound curve, relative to the baseline curve, was adopted as shown in Figure 2. The upper and lower bound curves for the tension hardening and tension softening regions have the same stiffness as the baseline curve and represent a roughly 15% increase and decrease in stress at first cracking and peak cracking strength. Twenty stiffness reductions (similar to damage states) resulted to represent the full stress strain response. The grey triangles in Figure 2 highlight the preservation of fracture energy dissipation using the sawtooth model, whereby the triangle above the baseline curve is "extra" energy dissipated by loading along E2 up to the upperbound curve, and the triangle below the curve is the "missing" energy dissipation upon reloading along E3, again to the upperbound curve. These two triangles are roughly equal, thus allowing for the preservation of fracture energy dissipation with reasonable accuracy. Again, a shear retention factor of 0.05 was adopted and Poisson's ratio was taken as 0.15. The linear analyses were run in load control as explained above and were repeated for 2000 steps.

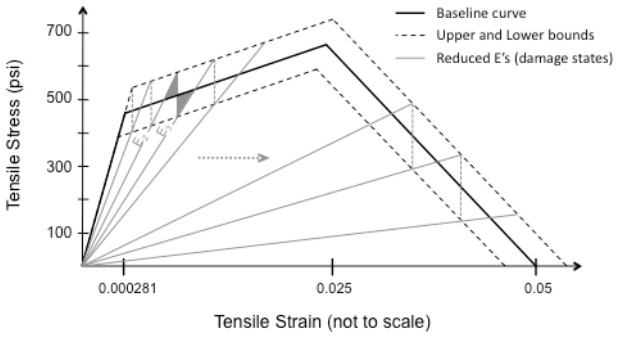

Figure 2. Saw-tooth tensile hardening-softening model for ECC *(100 psi =0.69MPa)*

Figure 3 compares the load-displacement response of the nonlinear analysis, the sequentially linear analysis and the three experiments on the ECC beams. The nonlinear analysis failed to converge in the second step after the peak load was reached (i.e. at a load of 141 lbs (627 N) and displacement of 0.25 in. (6.4

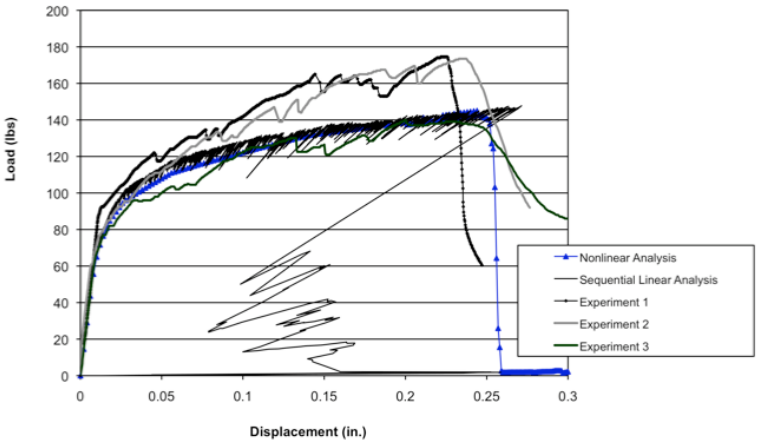

Figure 3. Load vs. Displacement of ECC beams and Analyses (*1 in. = 25.4 mm; 1 lb = 4.45 N)*

mm) and did not converge again until the load was essentially zero. This point of lack of convergence coincided with the first integration point to reach the softening branch of the ECC constitutive model. The sequential linear analysis is able to capture the likely snap-back experienced during failure. The test set-up was not able to capture snapback and therefore direct comparisons cannot be made.

Figure 4 compares the principal tensile strain contours at the last converged step at a load of 141 lbs (627 N) and displacement of 0.25 in. (6.4 mm) in the nonlinear analysis and at the same displacement and load pair for the sequentially linear analysis. The colors in Figure 4 represent different regions in the ECC tensile strain response as labeled in the figure. Both analysis methods show that at this displacement, the ECC has experienced significant multiple cracking and is just beginning to reach the softening branch.

Figure 5 shows the same principal tensile strain contours after the load has reduced to zero for each analysis method (and at equal displacements) with the same contour definitions as in Figure 4. Here it can be seen that a single, dominant crack has formed in the ECC in the constant moment region for each beam, although in slightly different locations, to roughly the same extent (height). Furthermore it can be seen in both analysis methods that as the ECC begins to form one dominant crack, the rest of the beam unloads and some of the previously cracked (hardening) region now experiences only elastic strain levels. Such unloading and closing of cracks is also observed experimentally.

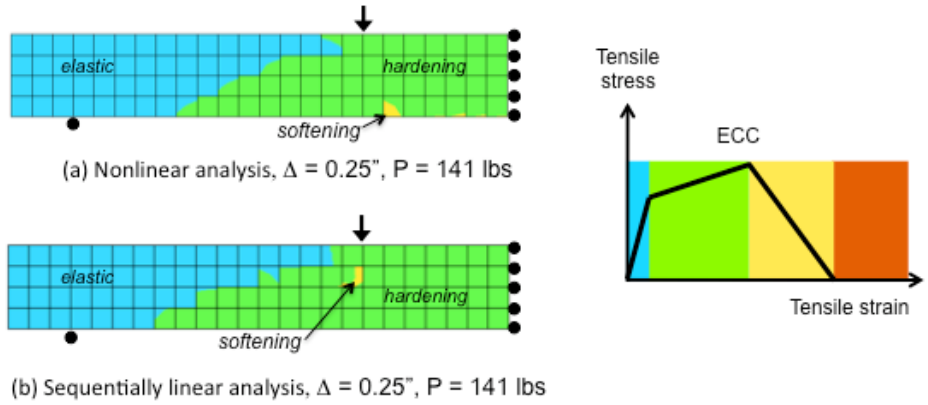

Figure 4. Principal tensile strain contours in ECC beams at last converged step for the nonlinear analysis *(1 in. = 25.4 mm; 1 lb = 4.45 N)*

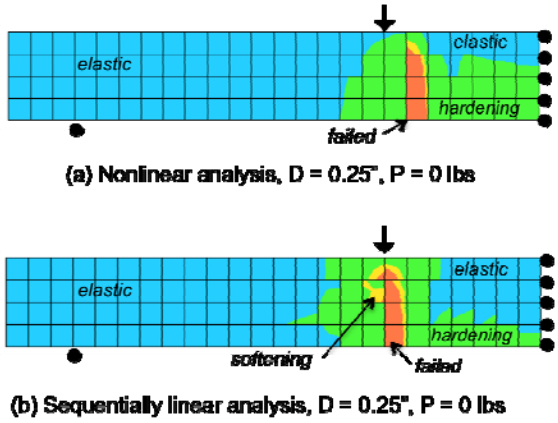

Figure 5. Principal tensile strain contours in ECC beams at failure ***(1 in. = 25.4 mm; 1 lb = 4.45 N)***

In Figure 6, the mesh sensitivity of the sequentially linear analysis is observed when comparing the original analysis (mesh of Figures 4-5) with an analysis performed on a beam with twice as many elements in each direction. Adopting the same saw-tooth softening model as for the original mesh, one would expect to see a more brittle response using the fine mesh, which is observed in Figure 6. A regularization procedure for tensile hardening-softening materials is needed.

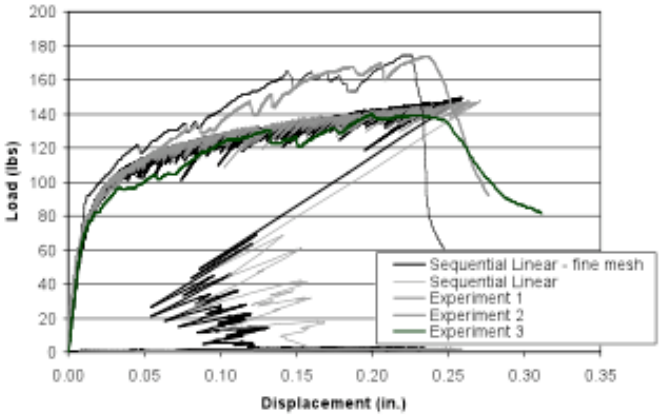

Figure 6. Load vs. Displacement of ECC beams from sequential linear analysis and two mesh sizes. *(1 in. = 25.4 mm; 1 lb = 4.45 N)*

4 SUMMARY & CONCLUSIONS

The flexural response of small-scale beams of ECC were simulated using two different analysis methods: nonlinear finite element analysis with a smeared, fixed crack model based on total strain, and sequential linear finite element analysis. It was found that both the nonlinear and sequential linear analysis methods predict well the load-displacement response of the deflection hardening ECC beams, using a tensile hardening-softening crack model. In both analyses, similar extents of multiple cracking were observed and softening of the ECC began at the same displacement (and load). A single, localized crack formed in both analyses to the same extent although in slightly different locations within the constant-moment region. Upon localization of the single dominant crack and unloading of the beam, the regions of the beam that had been tensile-hardening also unloaded in both analyses, as observed in experiments.

The sequential linear analysis was able to capture likely snapback behavior after crack localization. In the nonlinear analysis, a more advanced solution procedure would be required to capture the snap back. Measuring snap back in the experiments was not attempted, and further effort to capture this behavior in the nonlinear analysis was not pursued here. Mesh dependence was observed in the sequential linear analysis for the ECC beams, as the adopted crack model was not regularized for mesh size. A regularization procedure for tensile hardening-softening materials is required.

5 REFERENCES

Feenstra, P.H., Rots, J.G., Arnesen A., Teigen, J.G., Hoiseth, K.V. (1998) "A 3D constitutive model for concrete based on a con-rotational concept," *Computational Modelling of Concrete Structures, Proceedings of EURO-C 1998*, de Borst, Bicanic, Mang & Meschke (eds), Balkema, Rotterdam, 13-22.

Lee, W.K. and S.L. Billington (2008) "Simulation of Self-Centering Fiber-Reinforced Concrete Columns," *Proceedings of ICE, Engineering and Computational Mechanics*, **161**(2): 77-84.

Rots, J.G. and S. Invernizzi (2004) "Regularized sequentially linear saw-tooth softening model." *International Journal for Numerical and Analytical Methods in Geomechanics*, **28**:821-856.

Rots, J.G., Belletti, B., and S. Invernizzi (2006) "Event-by-event strategies for modelling concrete structures," *Computational Modelling of Concrete Structures, Proceedings of EURO-C 2006* Meschke, de Borst, Mang & Bicanic (eds), Taylor & Francis Group, London, 667-678.

Simulation of intralaminar and interlaminar failure mechanisms in laminated polymer-based composite materials.

P.P. Camanho
DEMec, Faculdade de Engenharia, Universidade do Porto
Rua Dr. Roberto Frias, 4200-465 Porto, Portugal

Keywords: Composite laminates; Delamination; Interlaminar Damage; Cohesive Zone Model; Continuum Damage Mechanics.

1 INTRODUCTION

Advanced analysis tools are essential for the introduction of optimized composite structures in the aerospace, railway, civil construction and automotive industries. It is well-know that accurate analysis tools enable the reduction of both recurring and non-recurring costs of composite structures. However, such tools are also required to understand the causes of structural collapse of composite structures [1], and to expand the design envelope of composite materials introducing new concepts such as variable stiffness panels [2] and hybrid composites [3].

The failure mechanisms of composite materials are inherently complex: as shown in Figure 1, the cross-section of a carbon-epoxy laminate exhibit both ply failure mechanisms such as fibre kinking, matrix transverse cracking and interfacial failure mechanisms (delamination).

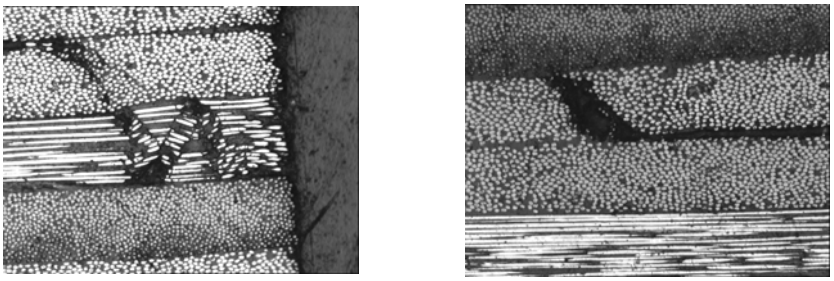

Figure 1: Failure mechanisms in carbon-epoxy composite laminates [4]

In addition, the polymer matrix exhibits a rate-dependent, viscoplastic response that is reflected in the response of each ply for particular loading directions (e.g. transverse compression, in-plane shear, longitudinal compression).

The difficulty predicting the response of polymer composites under complex load paths has prompted several research groups to develop a systematic approach to develop new analysis models. This work will present an overview of the main aspects of some models that were pro-

posed to predict the onset and propagation of the different failure mechanisms, intralaminar and interlaminar, as well as the interactions of thereof.

2 INTRALAMINAR FAILURE MECHANISMS

The main difficulties in the prediction of intralaminar failure mechanisms are: i) the choice of appropriate failure criteria to predict the different, fibre-dominated or matrix dominated, failure mechanisms; ii) the prediction of the actual strength of a composite ply when it is embedded in a multiaxial laminate (in-situ effect); iii) the definition of the damage evolution law (or cohesive laws). Besides, the difficulties previously outlined (at the constitutive level), the numerical implementation of strain-softening material models adds additional problems such as mesh dependence (in terms of element size and crack propagation path), and extremely slow convergence rates.

To overcome some of the difficulties outlined above, a systematic approach was taken to address each one of them and, in a 'building-block' approach, define a continuum damage model for intralaminar failure mechanisms. Therefore, analytical models, based on Fracture Mechanics analyses of cracked plies, were proposed to determine the actual strengths of a ply when embedded in a multidirectional laminate [5]. In addition, new failure criteria, the LaRC failure criteria that place a special focus in the fibre kinking and transverse compression failure modes, were proposed [6]. The LaRC failure criteria and the concepts of in-situ strengths are the basis of a continuum damage model that predicts not only the onset of the different failure mechanisms but also their propagation up to structural collapse [7-8].

One fundamental aspect of the continuum damage model that is often overlooked is the need to define a bi-linear, or linear-exponential, softening law for fibre-dominated failure mechanisms. The complex energy dissipation mechanisms at the crack tip and along the fracture process zone cannot be represented with a simple linear softening law. This fact is evident examining Figure 2 where the load-displacement relation of a compact tension test specimen predicted using linear and bi-linear softening laws are compared with the corresponding experimental data [9]. It is clear that the simple linear cohesive law severely over predicts the peak load.

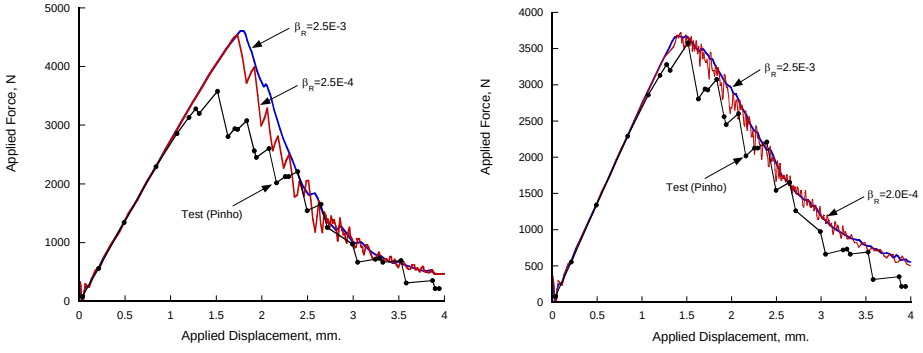

a) linear softening law b) bi-linear softening law

Figure 2: Load-displacement relations for a compact tension test specimen [9].

3 INTERLAMINAR FAILURE MECHANISMS

Cohesive zone models are ideal analysis methods to simulate the onset and propagation of delamination. In fact, the possible planes of delamination onset and growth are known in advance as they correspond to the interfaces between the different plies. When using cohesive zone models it is assumed that the inelastic mechanisms that precede the propagation of delamination are lumped to a surface ahead of the crack tip (Figure 3). The fracture process zone that develops ahead of the crack tip is represented by a relation between the tractions and the displacement jumps.

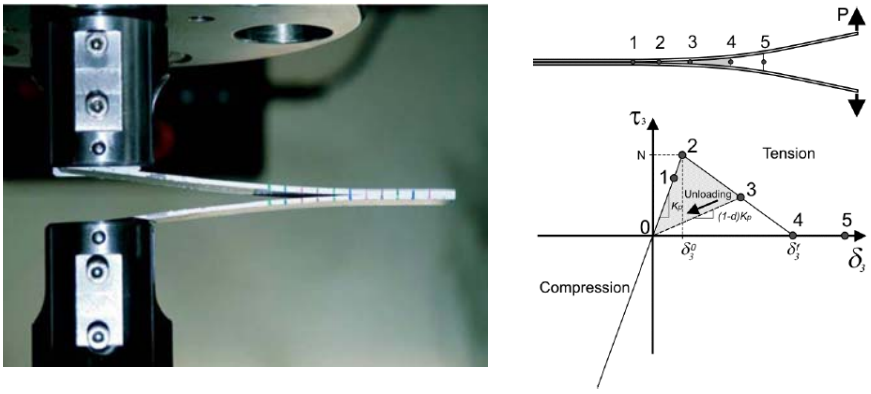

Figure 3: Cohesive zone model in the simulation of a delamination growing in mode I.

Cohesive zone models can be implemented in Finite Element Models using cohesive elements [10-11]. A fundamental aspect for the accurate simulation of delamination using cohesive elements is their ability to predict the fracture toughness under mixed-mode loading conditions. In other words, the element must correctly capture the energy release rates for the different loading modes, G_i (i=I, II, III), and use this information in an appropriate mixed-mode delamination propagation criterion. As shown in Figure 4 [12], whenever Linear-Fracture Mechanics (LEFM) conditions apply, i.e., for small fracture process zones, the solution obtained by the cohesive element must match the LEFM solution regardless of the values of the interlaminar strengths used in the model.

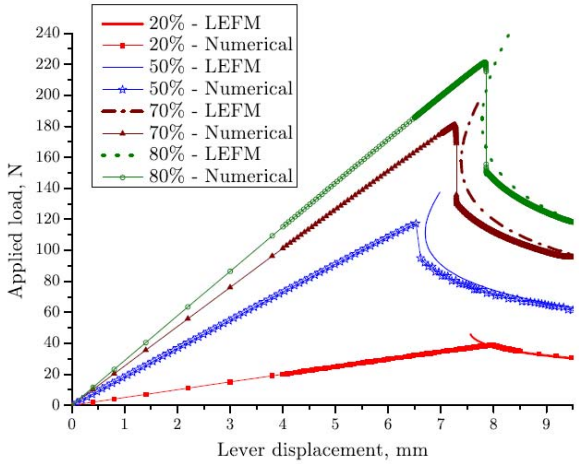

Figure 4: Analytical (LEFM) and numerical load-displacement curves for mixed-mode bending test specimens [12].

In general, structural failure occurs by a combination of both interlaminar and intralaminar failure mechanisms. Two different types of models that were developed to simulate this interaction are discussed: meso-models that combine cohesive elements with continuum elements [13] and a three-dimensional model for a transversely isotropic laminate that accounts for all failure mechanisms (Figure 5) [14].

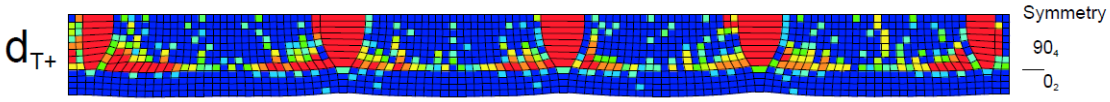

Figure 5: Simulation of transverse matrix cracks and delamiantion using a transversely isotropic damage model [14]

4 REFERENCES

[1] C.G. Dávila, P.P. Camanho, A. Turon, Effective simulation of delamination in aeronautical structures using shells and cohesive elements, Journal of Aircraft, 45, 663-672, 2008.

[2] C.S. Lopes, P.P. Camanho, Z. Gurdal, B.F. Tatting, Progressive failure analysis of tow-placed, variable-stiffness composite panels, International Journal of Solids and Structures, 44, 8493-8516, 2007.

[3] P.P. Camanho, A. Fink, A. Obst, S. Pimenta, Hybrid titanium-CFRP laminates for high-performance bolted joints, in press, Composites - Part A, 2009

[4] P.P. Camanho, Application of numerical methods to the strength prediction of mechanically fastened joints in composite laminates, PhD Thesis, Imperial College of Science, Technology and Medicine, University of London, U.K., 1999.

[5] P.P. Camanho, C.G. Dávila, S.T. Pinho, L. Iannucci, P. Robinson, Prediction of in-situ strengths and matrix cracking in composites under transverse tension and in-plane shear, Composites-Part A, 37, 164-176, 2006.

[6] C.G. Dávila, P.P. Camanho, C.A. Rose, Failure criteria for FRP laminates, Journal of Composite Materials, 39, 323-345, 2005.

[7] P. Maimí, P.P. Camanho, J.A. Mayugo, C.G. Dávila, A continuum damage model for composite laminates: part I- constitutive model, Mechanics of Materials, 39, 897-908, 2007.

[8] P. Maimí, P.P. Camanho, J.A. Mayugo, C.G. Dávila, A continuum damage model for composite laminates: part II- computational implementation and validation, Mechanics of Materials, 39, 909-919, 2007.

[9] C.G. Dávila, C.A. Rose, P.P. Camanho, R-curve toughening in the longitudinal fracture of composites and associated cohesive law, in press, International Journal of Fracture, 2009.

[10] P.P. Camanho, C.G. Dávila, M.F. de Moura, Numerical simulation of mixed-mode progressive delamination in composite materials, Journal of Composite Materials, 37, 1415-1438, 2003.

[11] A. Turon, P.P. Camanho, J. Costa, C.G. Dávila, A Damage Model for the Simulation of Delamination in Advanced Composites under Variable-Mode Loading, Mechanics of Materials, 38, 1072-1089, 2006.

[12] A. Turon, P.P. Camanho, J. Costa, J. Renart, Accurate simulation of delamination growthunder mixed-mode loading using cohesive elements: definition of interlaminar strengths and elastic stiffness, in press, Journal of Composite Materials, 2009.

[13] C.S. Lopes, P.P. Camanho, Z. Gurdal, P. Maimí, E. González, Low-velocity impact damage on dispersed stacking sequence laminates. Part II: numerical simulations, Composites Science and Technology, 69, 927-947, 2009.

[14] P. Maimí, P.P. Camanho, J.A. Mayugo, A three-dimensional damage model for transversely isotropic composite laminates, Journal of Composite Materials, 42, 2717-2745, 2008.

Microplane model reflecting both initial and damage-induced anisotropy and its applicability to textile reinforced concrete

R. Chudoba
A. Scholzen
J. Hegger

Institute of Structural Concrete, RWTH Aachen, Germany

keywords: *anisotropic damage, continuously reinforced cementitious composites,*

INTRODUCTION

Due to the variety of possible material layouts of the cementitious composites, maximum flexibility of the damage model is required in order to reflect the diversity of possible damage patterns. This flexibility is given by anisotropic damage models explicitly relating the damage laws to particular geometrical direction. Such formulations are generally referred to as **microplane models**. In this paper a microplane model is used in a form enhanced with initial anisotropy. In such a form it is particularly suitable for the simulation of quasi-ductile composites combining continuous and short-random reinforcement. The present paper will set the selected approach into the general context of damage modeling and presents verification studies using the model, including the comparison with the measured response of textile-reinforced concrete specimens.

BRIEF CLASSIFICATION OF MICROPLANE MODELS

The basic steps in the formulation of a microplane model are schematically depicted in Fig. 1 (a) for an early formulations of the microplane model including softening [BAZ84]:

- geometric projection of the macroscopic strain tensor ε_{ij} to obtain the corresponding microplane strain vectors e_i
- evaluation of constitutive laws at the microplane level
- an energetic homogenization of the microplane stress vectors s_i to obtain the macroscopic stress tensor σ_{ij} .

The first microplane model as described in [BAZ85] was limited in its ability to reproduce the linear-elastic case and allowed only a certain range of values for the Poisson's ratio Fig. 1 (a).. This unnatural restriction was eliminated in the succeeding models [BAZ88] by splitting the microplane normal strains and stresses into a volumetric (e_V, s_V) and deviatoric part (e_D, s_D). The basic scheme of this class of microplane models is depicted in Fig. 1 (b). The shear component of the microplane strain/stress vectors (e_i, s_i) is denoted in the Figure by (e_T, s_T). The introduction of the split leads to the correct reproduction of arbitrary values of Poisson's ratio as well as a better behavior under triaxial compression. Despite of these improvements and convincing practical applicability of the model in terms of good fits and prediction of experimental behavior [BAZ00] for wide range of loading cases, this version of the model did not fulfill the re-

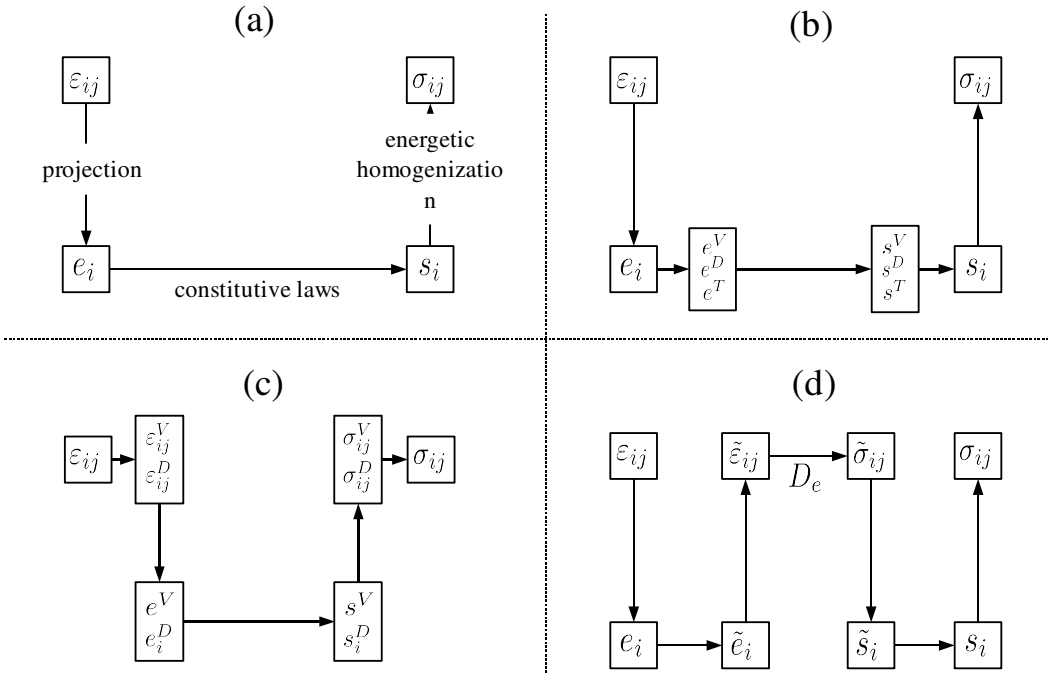

Figure 1: Classification of different types of microplane models: (a) basic principle of the microplane approach; (b) microplane formulation with split on the microplane level; (c) microplane formulation with split on the macroscopic level; (d) microplane formulation with explicit representation of the elasticity tensor.

quirement on thermodynamic consistency. On the other hand, if the split is introduced directly at the macroscopic level Fig. 1 (c) instead of the microplane level it leads to a thermodynamically consistent formulation.

An alternative formulation Fig. 1 (d) that does not need the split was provided in [JIR99]. In contrast to the original microplane scheme in Fig. 1 (a) the connection between the effective macroscopic strain tensor $\tilde{\varepsilon}_{ij}$ and stress tensor $\tilde{\sigma}_{ij}$ is established explicitly using the elasticity tensor D_e. This places this microplane model into the context of classical damage mechanics. For undamaged material the model can exactly reproduce the linear-elastic response. Furthermore, the Poison's effect is correctly reproduced for arbitrary values of the Poison's ratio.

DIRECTION-DEPENDENT DAMAGE FUNCTION

The model [JIR99] has been utilized here to include direction-dependent damage functions reflecting initial and damage induced anisotropy. The direction-dependent parameters are defined exploiting the explicit notion of microplane orientation. The damage state of a microplane is described by the damage parameter ω_i, respectively the integrity parameter $\phi_i = (1 - \omega)$, which is obtained as a function of the maximum equivalent microplane strain e_{max} reached on the corresponding microplane in the loading history. The damage function can be defined applying an exponential softening law as indicated in Eq. (1). The parameter e_p controls the transition between the elastic and inelastic regime and the parameter e_f the initial slope of the softening curve.

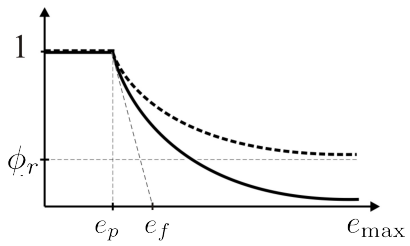

Figure 2: Damage functions for quasi- brittle (solid line) and quasi-ductile (dashed line) behavior.

$$\phi = f(e_{\max}) = \begin{cases} 1 & \text{if} \quad e_{\max} < e_p \\ (1-\phi_r)\sqrt{\frac{e_p}{e_{\max}}}\exp\left(-\frac{e_{\max}-e_p}{e_f-e_p}\right) + \phi_r & \text{if} \quad e_{\max} \geq e_p \end{cases} \tag{1}$$

In order to reflect the quasi-ductile effect of the reinforcement, the damage law corresponding to the reinforced direction must show a residual integrity. In the preliminary version of the model, this has been implemented by introducing the variable $\phi_r = 0.40$ into the damage law representing the horizontal asymptote at the desired level of residual integrity. In the case of a quasi-brittle material ϕ_r tends towards zero (cf. Fig. 2). The residual integrity has been set for the microplanes oriented within the range $\pm\pi/8$ from the reinforced direction. From that point on, ϕ_r decreases linearly to zero for the direction perpendicular to the reinforcement.

SIMULATION OF TENSILE SPECIMEN WITH INCLINED REINFORCEMENT

Besides the damage induced anisotropy, the material model at the macroscopic level must be able to capture the effect of initial anisotropy on the response for varied loading directions, including the case of non-proportional loading. Fig. 3 exemplifies the model response for an initially anisotropic material. In the example the inclination of the reinforcement (indicated by the thick gray lines) with respect to the loading direction (indicated by the arrows) is varied and the macroscopic response evaluated.

For the case of loading disk in the reinforced direction ($\alpha = 0$, first row in Fig. 3) the composite exhibits multiple cracking in terms of a pronounced strain hardening in the response curve. The same disk loaded perpendicularly to the reinforcement ($\alpha = \frac{\pi}{2}$, last row in Fig. 3) exhibits the strain softening response of plain concrete. The transition between these two extreme cases is illustrated in the second and third row for angles $\alpha = \frac{\pi}{16}$, $\alpha = \frac{\pi}{8}$. In the former case of small inclination, the stress-strain-diagram is almost identical to the case $\alpha = 0$, only a slight decrease of the stiffness can be recognized after the formation of cracks has finished. For $\alpha = \frac{\pi}{8}$ the tension stiffening effect is less pronounced and the stiffness is further reduced as compared to the cases with aligned reinforcement. The sudden drop of stress at the strain level of 0.15% corresponds to the failure of microplanes in the unreinforced direction. The neighboring “reinforced” microplanes are still able to transfer the tensile stresses and prevent the ultimate failure.

Further aspects of the model behavior and comparison with experimental response of a tensile test with varied inclination of the reinforcement shall be given in the presentation.

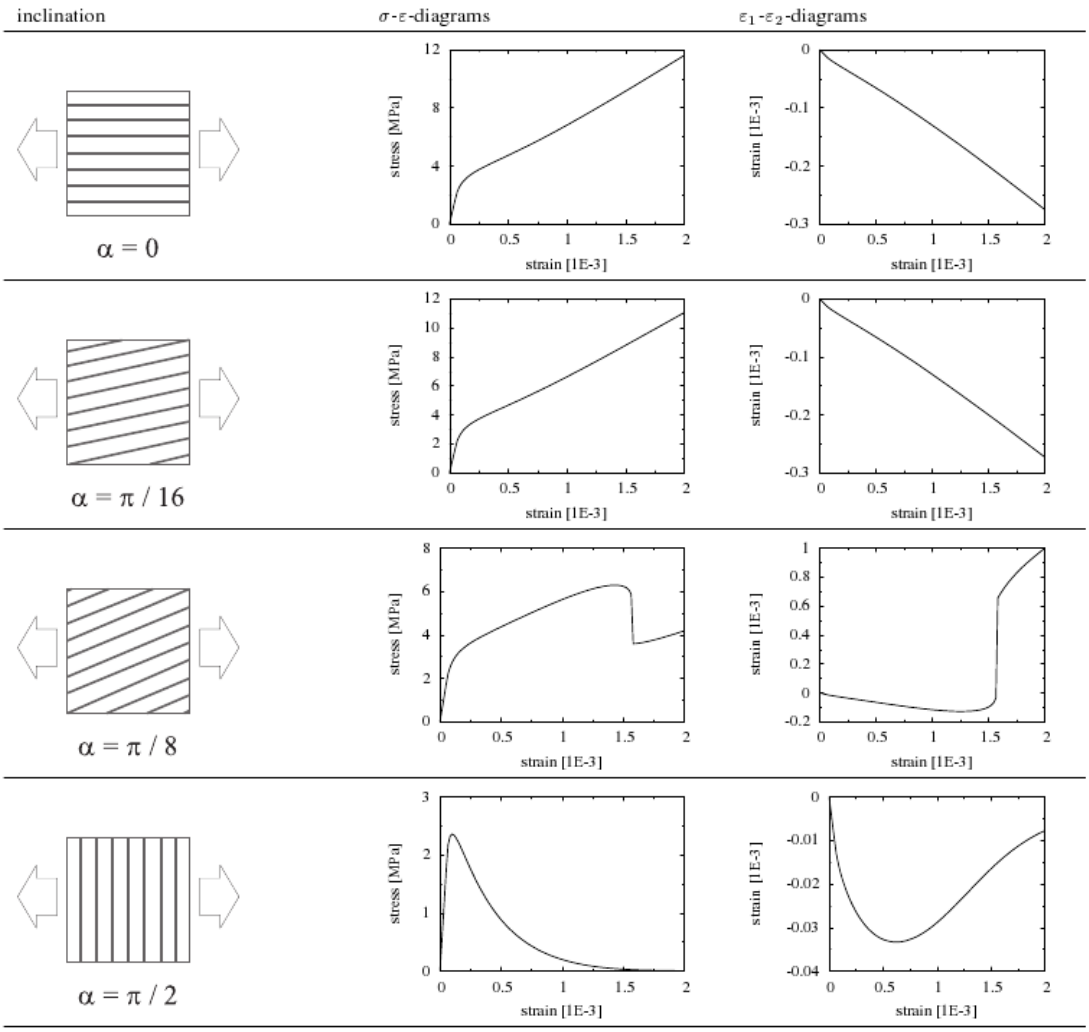

Figure 3: Simulated response of the composite for varied inclinations of the reinforcement; First column: reinforcement inclination; Second column: stress – strain response; Third column: development of the lateral strain versus control strain in the loading direction.

REFERENCES

[BAZ84]	Bazant, Z.P.; Gambarova, P.G.	Crack shear in concrete: crack band microplane model. *J. Struct. Engng., ASCE 110,* 2015-2036, 1984.
[BAZ85]	Bazant, Z.P.; Oh, B.-H.	Microplane model for progressive fracture of concrete and rock. *Journal of Engineering Mechanics*, ASCE, 111(4), 559-582, 1985.
[BAZ88]	Bazant, Z.P.; Prat, P.C.	Microplane model for brittle material. I: Theory. *Journal of Engineering Mechanics*, ASCE, 113(7), 1050-1064, 1987.
[JIR99]	Jirasek, M.	Comments on microplane theory. *Mechanics of Quasibrittle Materials and Structures, Hermes Science Publications, Paris, S. 55-77,* 1999.
[SCH08]	Scholzen, A.; Chudoba, R.; Hegger, J.;	Numerical simulation of TRC using microplane-type model with initial anisotropy, In: *Ninth International Conference on Computational Structures Technology (CST2008)*, Athens, Greece, CD-ROM (14 pages), 2008.

Coupled analysis of building damage due to tunnelling

G. Giardina
Delft University of Technology, The Netherlands

M.A.N. Hendriks
Delft University of Technology, The Netherlands

J.G. Rots
Delft University of Technology, The Netherlands

Keywords: Damage assessment, masonry building, tunneling.

1 INTRODUCTION

Excavation works in urban areas require a preliminary risk damage assessment. In historical cities, the prediction of building response to settlements is necessary to reduce the risk of damage of the architectural heritage. The current method used to predict the building damage due to ground deformations is the Limiting Tensile Strain Method (LTSM) [3]. This method is based on an uncoupled soil-structure analysis, in which the building is modelled as an elastic beam subject to imposed greenfield settlements and the induced tensile strains are compared with a limit value for the material. This approach neglects many factors which play an important rule in the response of the structure to tunneling induced settlements.

In this paper, the possibility to apply a settlement risk assessment derived from the seismic vulnerability approach [1] is considered. The parameters that influence the structural response to settlements can be defined through numerical coupled analyses which take into account the nonlinear behaviour of masonry and the soil-structure interaction.

2 DAMAGE CLASSIFICATION SYSTEM

The Limiting Tensile Strain Method is an empirical analytical method currently used in engineering practice to predict building damage due to settlements. In this approach, the greenfield ground movements are projected on the structure represented as a linear elastic beam, with an equivalent shear and bending stiffness (Fig.1a). A fictitious point load causing the greenfield deflection on the simple supported beam is calculated, and the induced tensile strains are derived (Fig.1b). The maximum total strain value is related to the expected damage level (Fig.1c).

The LTSM is based on significant simplifications: the nonlinear behaviour of the structural material is neglected, and no interaction between the soil and the building is considered. [4]

Based on the principles of the seismic vulnerability assessment, the sensitivity of a certain building typology to be damaged by a differential settlement of a given magnitude could be described by a susceptibility index s, which can take into account different parameters like material properties, type of foundations, geometry, amount of openings, previous damage. A typical formulation of this index can be:

$$s = \sum_{i=1}^{n} w_i p_i$$

where n is the number of the considered parameters and w_i and p_i are the weight and the value of the i-th parameter, respectively. In this work, the numerical analyses used to evaluate the weight and the value of some of the most significant parameters are described.

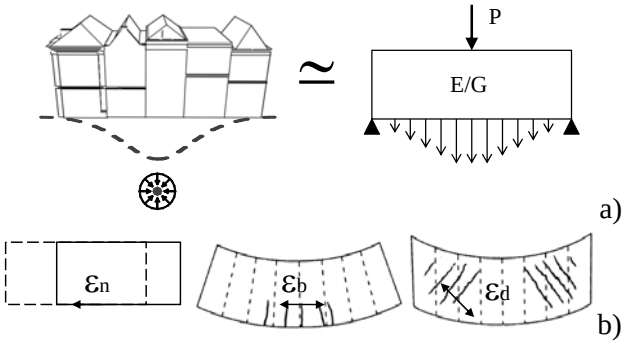

Dam. level	Damage class	Crack width w	Tensile strain ε
0	Negligible	<0.1mm	0-0.05
1	Very slight	<1mm	0.05-0.075
2	Slight	<5mm	0.075-0.15
3	Moderate	5-15mm	0.15-0.3
4-5	Severe/Very severe	>25mm	>0.3

c)

Fig.1. LTSM procedure: a) building schematization, b) tensile strains calculation, c) damage assessment.

3 NUMERICAL ANALYSIS

The situation modelled in this work represents the typical conditions of a tunnel excavation in Amsterdam. An historical building on pile foundations driven in soft soil is located above the tunneling situ (Fig.2a).

The masonry façade is modelled with eight node quadrilateral plane stress elements, with a three by three point integration scheme. A total-strain rotating crack model with a linear softening diagram simulates the material behaviour (Fig.3c). The facade is subjected to dead and live loads (Fig.2b).

The interaction between soil and wall is modelled with quadratic line interface elements; the normal stiffness of the interface in compression is derived from geotechnical considerations, taken into account the combined stiffness of the wooden pile foundations and the soft soil. Its value is $D_n=1.1*10^9$ N/m^3. A no tension criterion in the normal direction is assumed. The slipping motion across the interface is governed by the shear stiffness. Two different cases are considered, in order to evaluate the influence of the transmission of the horizontal ground deformations to the building. A shear stiffness modulus of $D_s=1*10^8$ N/m^3 and a Coulomb friction criterion (Fig.3f) are adopted for the so called rough interface, while a reduced shear stiffness of $D_s=1$ N/m^3 and no friction criterion are included in the smooth case.

The soil is modelled with six node triangular plane strain elements; it's considered linear elastic, with a Young's modulus increasing with the depth (Fig.3d).

In order to simulate the volume loss caused by the tunnelling process, an increasing pressure is applied to the quadratic curved beams wich represent the tunnel lining [2].

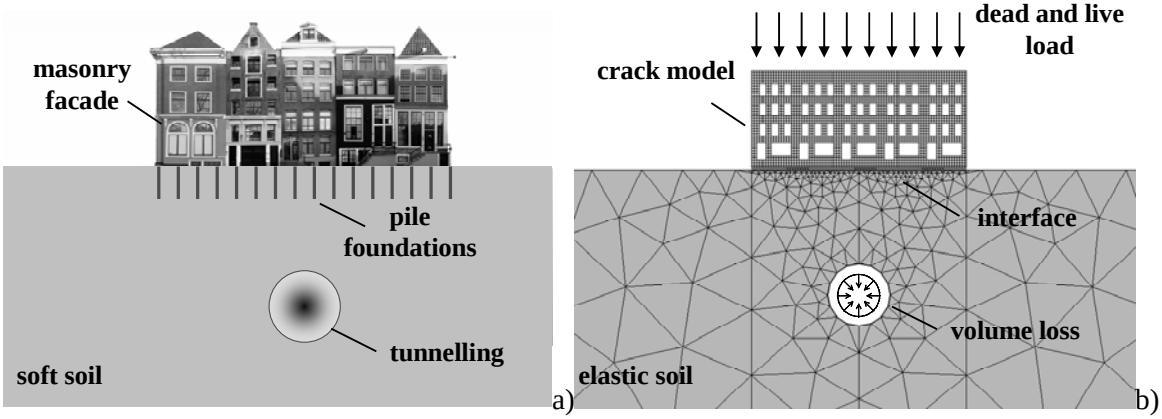

Fig.2. Coupled numerical modelling (b) of a typical Dutch tunnelling situation (a).

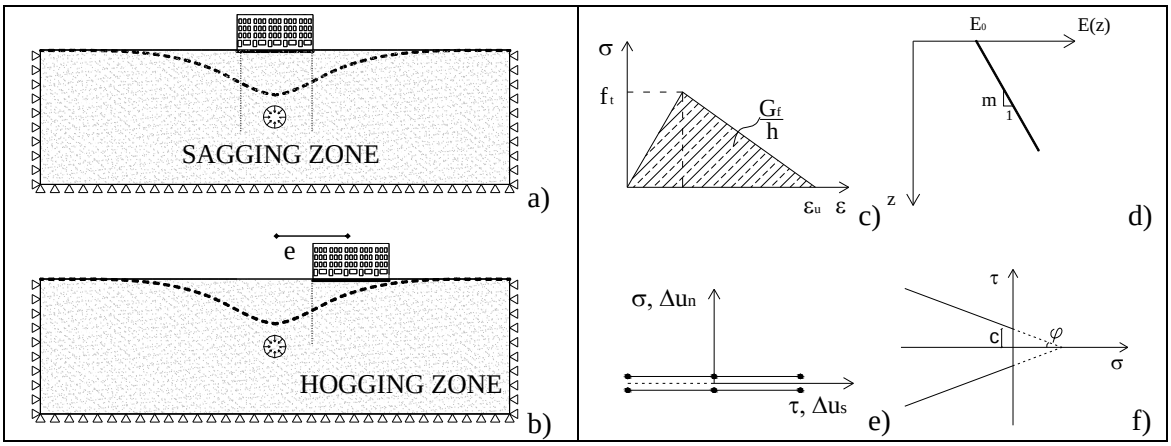

Fig.3. Numerical model: sagging (a) and hogging (b) case, constitutive lows for the materials (c, d, e, f).

The potential risk level is related not only to the magnitude of differencial settlement but also to the typical failure mechanism, wich is linked to a certain settlement profile. For this reason, the position of the building with respect to the tunnel is varied. In order to evaluate the influence of the openings (doors and windows) on the structural damage, the same analyses are performed also using a 2D model of a simple masonry wall.

4 RESULTS

The results of the coupled analysis are reported in terms of structural damage as function of tunnelling induced volume loss (Fig.6). The comparison indicates that buildings located in the hogging zone (Fig.4b,d) are more sensitive to be damaged than the ones in the sagging area (Fig4a,c), as empirical observation on real cases show [3], only if the possibility to transmit the horizontal deformations from the ground to the structure is taken into account (rough interface). This means that the soil-structure interaction has a sensitive effect on the development of a certain damage mechanism. The comparison between the simple wall and the façade response reveal a strong influence of the openings, not only in terms of reduced stiffness but also regarding the fracture localization. In fact, the façade is more flexible to the imposed settlements, resulting in a reduced damaged at the same value of volume loss (Fig.6), and the presence of the windows lead to a different crack pattern development (Fig.5).

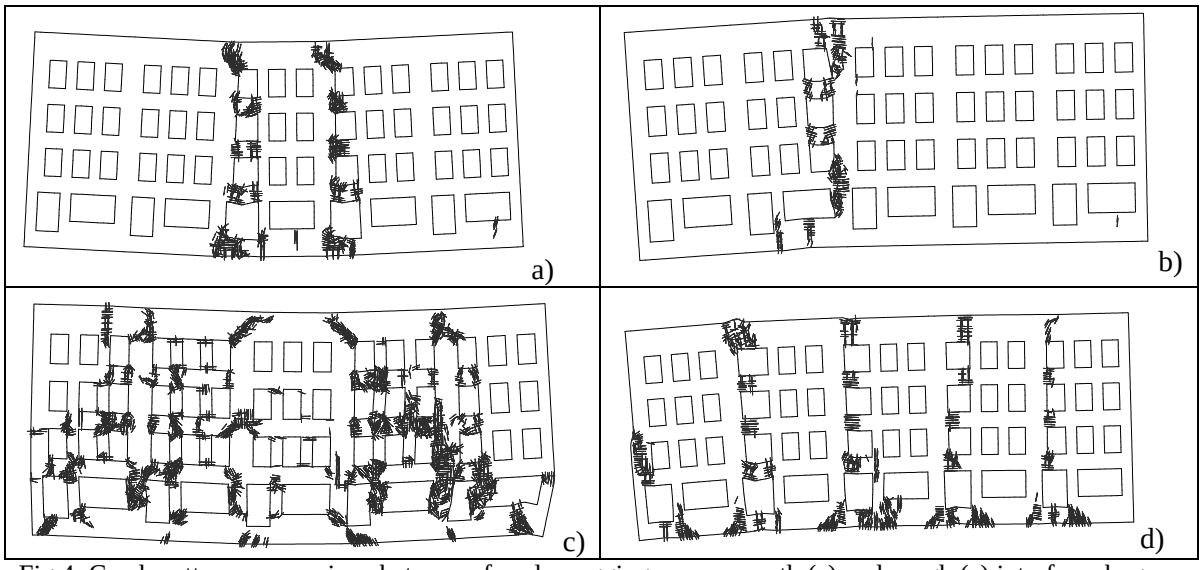

Fig.4. Crack pattern, comparison between: façade, sagging zone, smooth (a) and rough (c) interface; hogging zone, smooth (b) and rough (d) interface.

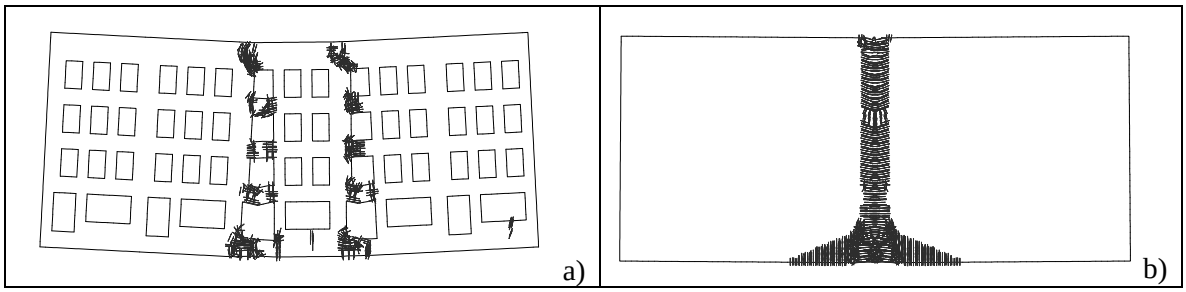

Fig.5. Crack pattern, comparison between: sagging zone, smooth interface, façade with windows (a), wall without openings (b).

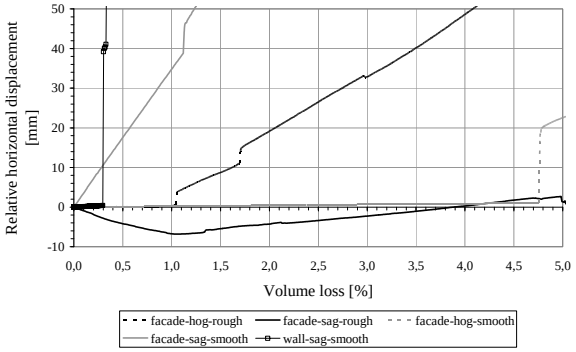

Fig.6. Comparison between the different coupled models in terms of relative horizontal displacements of the outer ends of the structure.

5 CONCLUSIONS

In the tunneling damage assessment of masonry buildings, many different parameters play an important role in the structural response. A damaged assessment based on the building sensitivity to building settlements could be adopted in the engineering practice.

Coupled numerical analyses reveal that the soil-structure interaction, the location with respect to the tunnel and the amount of openings have a significant influence on the building response, and therefore all this parameters need to be included in the sensitivity index with an high value of their relative weights.

REFERENCES

[1] Benedetti, D. and Petrini V., (1984). On seismic vulnerability of masonry buildings: proposal of an evaluation procedure, L'industria delle Costruzioni; volume 18: 66-78.

[2] Bloodworth A.G., (2002). Three-dimensional analysis of tunnelling effects on structures to develop design methods,PhD thesis, University of Oxford.

[3] Burland J.P. and Wroth C.P., (1974). Settlement of buildings and associated damage, Proceedings of Conference on Settlement of Structures, Pentech Press, Cambridge, pp. 611-654.

[4] Netzel H., (2009). Building response due to ground movements, PhD thesis, Delft University of Technology, Delft.

Sequentially linear analysis of masonry structures under non-proportional loading

A.V. van de Graaf
Delft University of Technology, Delft, The Netherlands

M.A.N. Hendriks
Delft University of Technology, Delft, The Netherlands

J.G. Rots
Delft University of Technology, Delft, The Netherlands

Keywords: sequentially linear analysis, non-proportional loading, masonry wall, shear test

1 INTRODUCTION

The development of sequentially linear analysis (SLA) was initiated by Rots and Invernizzi [1] in response to convergence difficulties which may arise when simulating fracture processes in large-scale brittle structures. Traditionally, a number of load-, displacement- or arc-length increments is considered. On top of that an iterative solution algorithm is employed to obtain equilibrium of the model given a predefined convergence criterion. However, due to highly nonlinear material behaviour full convergence may not be obtained for one or more steps.

The basic concept of SLA is to execute a series of linear analyses which are scaled afterwards such that a critical event – e.g. crack initiation in a point – is obtained. After each linear analysis a damage increment is applied to one critical integration point. Consequently, the tensile strain softening diagram needs to be discretized, resulting in a so-called saw-tooth diagram. The primary benefit of this technique is that it renders an iterative solution algorithm redundant, yielding a robust approach.

Recently this method was extended by DeJong et al. [2] to account for non-proportional loading. Contrary to proportional loading, non-proportional loading introduces its own difficulties. This contribution outlines these difficulties and attempts to gain insight into this matter.

2 ADAPTED FORMULATION FOR SEQUENTIALLY LINEAR ANALYSIS UNDER NON-PROPORTIONAL LOADING

Let load set *A* consist of all non-proportional loads and let load set *B* consist of all proportional loads. Assuming plane stress conditions, this yields, for every integration point, three stress components per load set, viz. $\sigma_{xx,A}$, $\sigma_{yy,A}$ and $\sigma_{xy,A}$ for load set *A* and $\sigma_{xx,B}$, $\sigma_{yy,B}$ and $\sigma_{xy,B}$ for load set *B*. By superimposing all stress components of load set *B* multiplied by a load multiplier λ to the corresponding stress components of load set *A*, the resulting stresses can be expressed as

$$\begin{aligned} \sigma_{xx} &= \sigma_{xx,A} + \lambda\sigma_{xx,B} \\ \sigma_{yy} &= \sigma_{yy,A} + \lambda\sigma_{yy,B} \\ \sigma_{xy} &= \sigma_{xy,A} + \lambda\sigma_{xy,B} \end{aligned} \tag{1}$$

For every integration point *i*, it should hold true that the maximum stress $\sigma_{\max}^{(i)}(\lambda)$ does not exceed the (current) tensile strength $f_t^{(i)}$, i.e.

$$\sigma_{\max}^{(i)}(\lambda) \leq f_t^{(i)} \tag{2}$$

In case integration point *i* is still un-cracked, $\sigma_{\max}^{(i)}(\lambda)$ is simply taken as the major principle stress $\sigma_1(\lambda)$ which can be calculated from the following well-known formula

$$\sigma_{1,2}(\lambda) = \tfrac{1}{2}\left(\sigma_{xx} + \sigma_{yy}\right) \pm \sqrt{\tfrac{1}{4}\left(\sigma_{xx} - \sigma_{yy}\right)^2 + \sigma_{xy}^2} \tag{3}$$

where σ_{xx}, σ_{yy} and σ_{xy} are to be taken from Eq. (1). The crack direction is fixed upon crack initiation ($\sigma_1(\lambda) = f_t$), i.e. a fixed crack model is adopted. In case integration point *i* was cracked in a previous step, $\sigma_{\max}^{(i)}(\lambda)$ is taken as the normal stress perpendicular to the crack face ($\sigma_{nn}(\lambda)$) which can be obtained through a stress transformation given the crack angle. To allow for secondary cracking perpendicular to the initial crack, also the normal stress parallel to the crack face ($\sigma_{tt}(\lambda)$) should be considered.

Solving the inequality in Eq. (2) yields a range of λ-values. Depending on the exact values of the stress components of load sets *A* and *B*, this range – also referred to as solution set – can be traced to one of the five general forms presented in Figure 1.

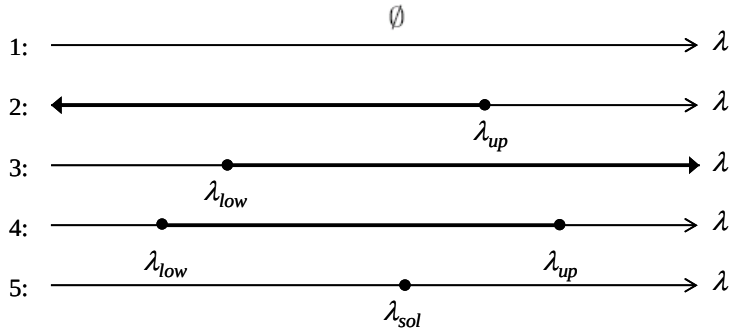

Figure 1 All five general solution forms of Eq. (2): empty solution set (1), upper-bounded semi-infinite solution set (2), lower-bounded semi-infinite solution set (3), closed solution set (4) and single-valued solution set (5).

So far, solution sets have been determined for every integration point individually. To identify the critical integration point, an overall solution set needs to be determined, i.e. find all common λ-values. Assuming that a non-empty overall solution set exists, its maximum value is selected as the critical load multiplier, as this represents the capacity for the current step. The integration point that delivered this critical load multiplier is selected as the critical integration point, i.e. its stiffness and strength are to be reduced in the next linear analysis.

However, also empty overall solution sets may be obtained. This means that no common load multiplier λ can be found such that Eq. (2) is satisfied for all integration points simultaneously. In that case a well-founded choice for the critical integration point is less obvious. Nevertheless, to continue SLA, a critical integration point has to be selected. A tentative solution – based on numerical observations – is to select the integration point yielding the lowest upper-bound. However, a more solid selection scheme would be desirable and therefore this phenomenon is subject of on-going research. In the next section the occurrence of an empty overall solution set is demonstrated for a masonry wall subjected to compressive and shear loading.

3 SIMULATION OF A DRY STONE MASONRY WALL UNDER COMPRESSIVE AND SHEAR LOADING

The structural behaviour of dry stone walls under a constant compressive loading and a gradually increasing shear loading has been investigated by Oliveira [3] by means of experiments and numerical simulations. In this contribution the same masonry wall is analyzed with SLA. The geometry of the wall, a schematic representation of the loading and the adopted material properties are given in Figure 2. All dimensions have been taken from Oliveira [3], except for the dimensions of the reinforced concrete beam which had to be estimated.

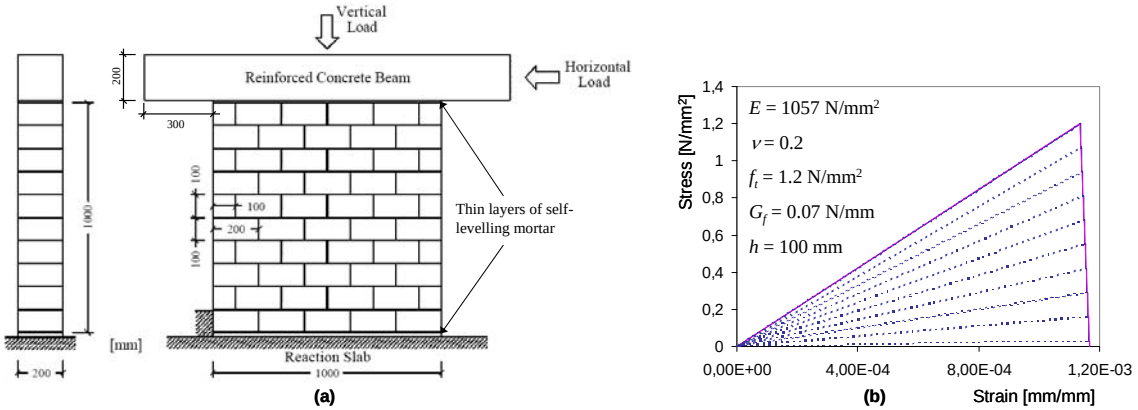

Figure 2 Geometry of the dry stone masonry wall and schematic loading arrangement by Oliveira [3] (a) and the adopted material behaviour – including saw-tooth diagram – of the masonry (b).

It is assumed that due to appropriate construction techniques out-of-plane failure of the wall is prevented. In other words, only in-plane structural behaviour is taken into account. Since the current implementation of SLA does not support physically nonlinear behaviour of interface elements, modeling the dry joints between the sandstone blocks has to be simplified. Therefore it was decided for the numerical analysis to define a homogenized material that represents the response of the bricks and joints in a smeared manner. The homogenized stiffness to be applied was calculated from experimental results and was found to be dependent on the level of compression. According to Oliveira [3] failure of the wall under a low compressive load level is primarily due to failure of the bed joints. However, as the compressive loading is increased, the failure pattern is more and more characterized by the occurrence of cracking of the stones. As it is expected that the latter failure mode can be predicted more easily by the adopted model, it was decided to take a vertical load of 200 kN. The corresponding Young's modulus of the wall is 1057 N/mm^2 (Oliveira [3]).

The procedure described in Section 2 works well up to and including step 170. In the next step an empty overall solution set is found. This can be visualized through contour plots of the upper and lower bounds of all integration points in the wall for step 171, see Figure 3. Clearly, the maximum lower bound is greater than the minimum upper bound. In Figure 4a it is shown that only one integration point has an upper bound smaller than the maximum lower bound. The stress flow for step 170 – displayed as a vector plot of the minor principle stress in Figure 4b – reveals that the lower right triangular part of the wall hardly contributes to the force flow. Figure 5 demonstrates that crack closing may occur. However, this kind of behaviour is not treated properly as the reduced stiffness is still used in the analysis. Ultimately, Figure 6 displays the obtained load-displacement diagrams. Note the sudden decrease in displacement just before step 171 (Figure 6a). Also note that the tentative selection scheme in case of an empty overall solution set gives unexpected results if the analysis is continued in this way (Figure 6b).

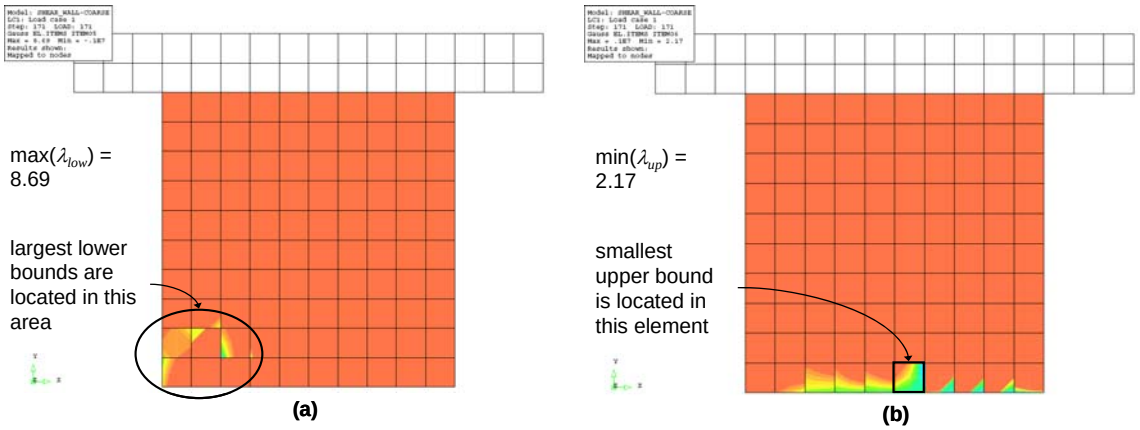

Figure 3 Contour plots of the lower bounds (a) and upper bounds (b) for step 171. The outlined element in (b) indicates the element which provides the minimum upper bound.

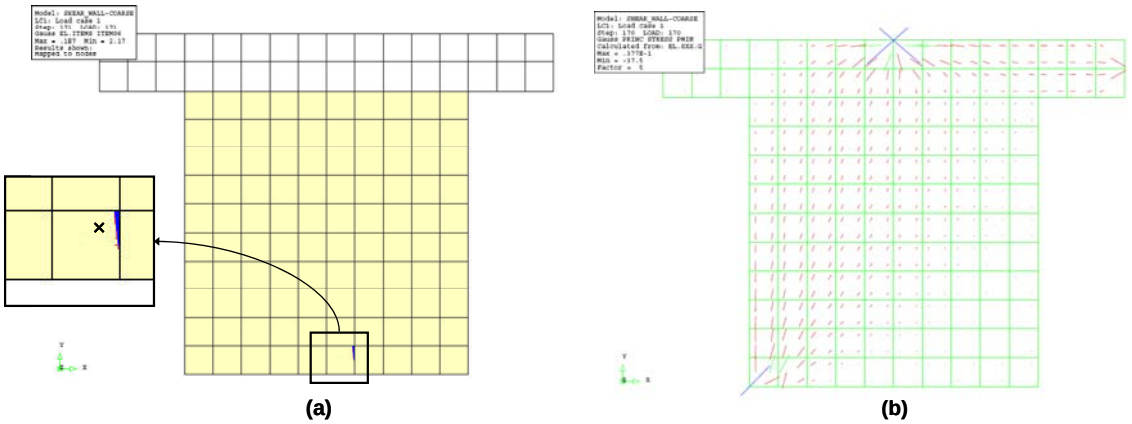

Figure 4 Contour plot showing in which part of the model the upper bound is smaller than the maximum lower bound (a) and a vector plot of the minor principal stress for step 170 (b).

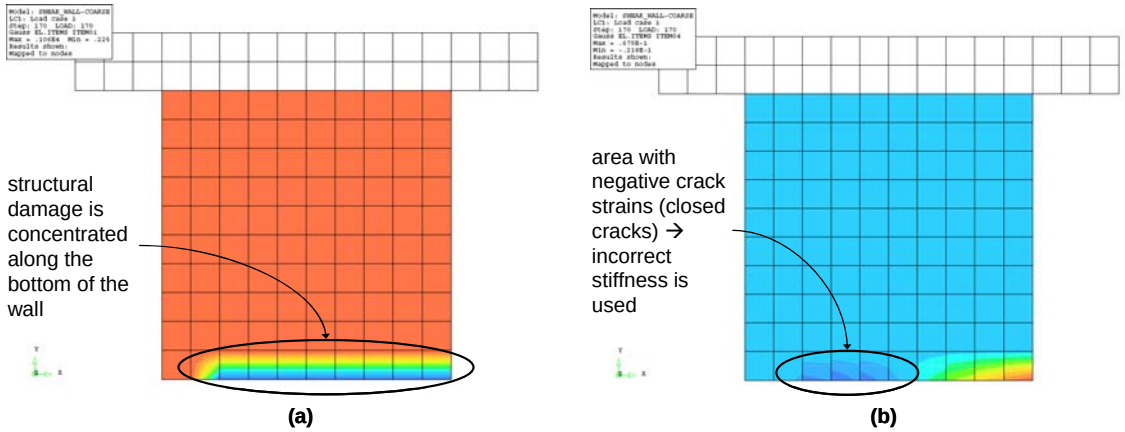

Figure 5 Contour plots of the (reduced) Young's modulus (a) and crack strains (b) for step 170.

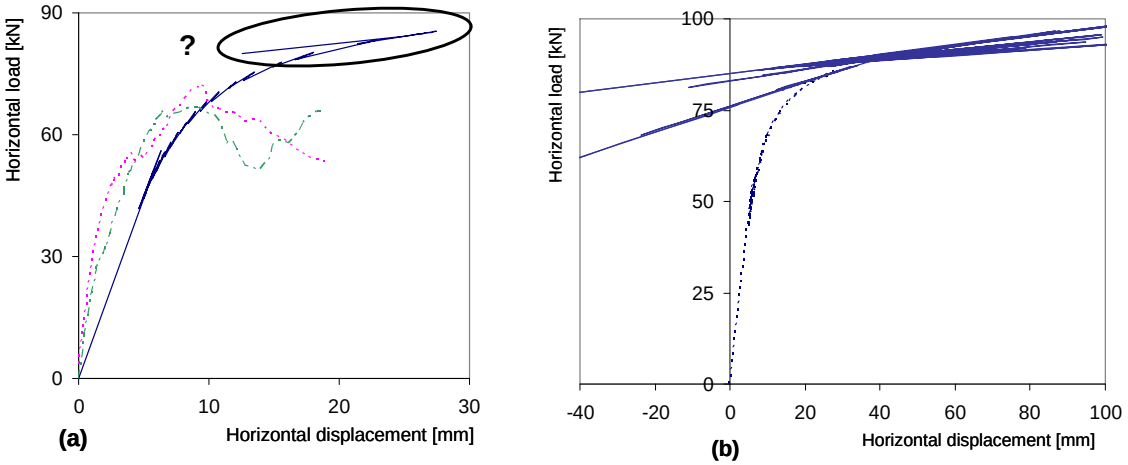

Figure 6 Horizontal load – horizontal displacement diagrams obtained with SLA (for steps 1-170, solid line) and experiments (dashed lines) (a). SLA results for steps 1-170 (dashed line) and steps 171-1000 (solid line) (b).

REFERENCES

[1] Rots JG, Invernizzi S. Regularized sequentially linear saw-tooth softening model. International Journal for Numerical and Analytical Methods in Geomechanics, 28 (2004), pp. 821-856.

[2] DeJong MJ, Hendriks MAN, Rots JG. Sequentially linear analysis of fracture under non-proportional loading. Engineering Fracture Mechanics 75 (2008), pp. 5042-5056.

[3] Oliveira DV. Experimental and numerical analysis of blocky masonry structures under cyclic loading. Ph.D. dissertation, Universidade do Minho, 2003.

Modeling Creep Induced Cracking Based on Piecewise Constant Damage and Relaxation Functions

Max A.N. Hendriks
Delft University of Technology, Faculty of Civil Engineering and Geosciences, Delft, The Netherlands

Jan G. Rots
Delft University of Technology, Faculty of Civil Engineering and Geosciences & Faculty of Architecture, Delft, The Netherlands

Keywords: sequentially linear analysis, creep, cracking, concrete

1 INTRODUCTION

Sequentially linear analysis is an alternative to non-linear finite element analysis of structures when bifurcation, snap-back or divergence problems arise. Sequentially linear analysis avoids convergence problems by directly specifying a damage increment instead of displacement or load increments. The method is based on the assumption of piecewise constant damage values, resulting in so-called saw-tooth tension softening diagrams. The present paper extends the method with a formulation for time dependent deformations, viz. creep [1].

2 CONSTITUTIVE MODELING

The constitutive model combines damage and creep in a multiplicative way. This formulation does not require a decomposition of the total strain into a creep strain and a crack strain. The stress – total strain history relation reads, Figure 1(a-c):

$$\boldsymbol{\sigma}(t) = (1-d)\int_0^t \frac{R(t,\tau)}{E}\mathbf{D}\frac{\partial \boldsymbol{\varepsilon}(\tau)}{\partial t}d\tau \tag{1}$$

The relaxation function or modulus $R(t,\tau)$ describes the stress evolution at time t due to a unit strain acting since time τ. It is scaled with a reference elastic modulus *E*. **D** denotes the material stiffness matrix and *d* is an isotropic damage state variable. Piecewise constant approximation of $R(t,\tau)$ with respect to both the loading age τ and the time t, based on N successive time intervals $[t_{i-1}, t_i]$, $i = 1,...,N$, gives

$$R_{ij} = R(\overline{t}_i, \overline{\tau}_j) \quad \text{for} \quad t_{i-1} < \overline{t} \le t_i, \quad t_{j-1} < \overline{\tau}_j \le t_j \tag{2}$$

where $\overline{\tau}_j = \frac{1}{2}(t_{j-1} + t_j)$ and $\overline{t}_i = \frac{1}{2}(t_{i-1} + t_i)$. The result of such a discretization is referred to as a series of downstairs relaxation functions R_{ij}. Figure 1(f) depicts the effect. Upon substitution of (2) in (1) we obtain, for the one-dimensional stress at time t_i

$$\sigma(t_i) = (1-d)\sum_{j=1}^{j=i} R_{ij}\Delta\varepsilon_j \tag{3}$$

where $\Delta\varepsilon_j = \varepsilon(t_j) - \varepsilon(t_{j-1})$. Piecewise constant approximation of d with respect to the internal variable α, viz. the maximum tensile strain, based on K successive intervals $[\alpha_{k-1}, \alpha_k]$, $k = 1,...,K$ is formulated as:

$$d_k(\alpha) = d(\overline{\alpha}_k) \quad \text{for} \quad \alpha_{k-1} < \alpha \le \alpha_k \tag{4}$$

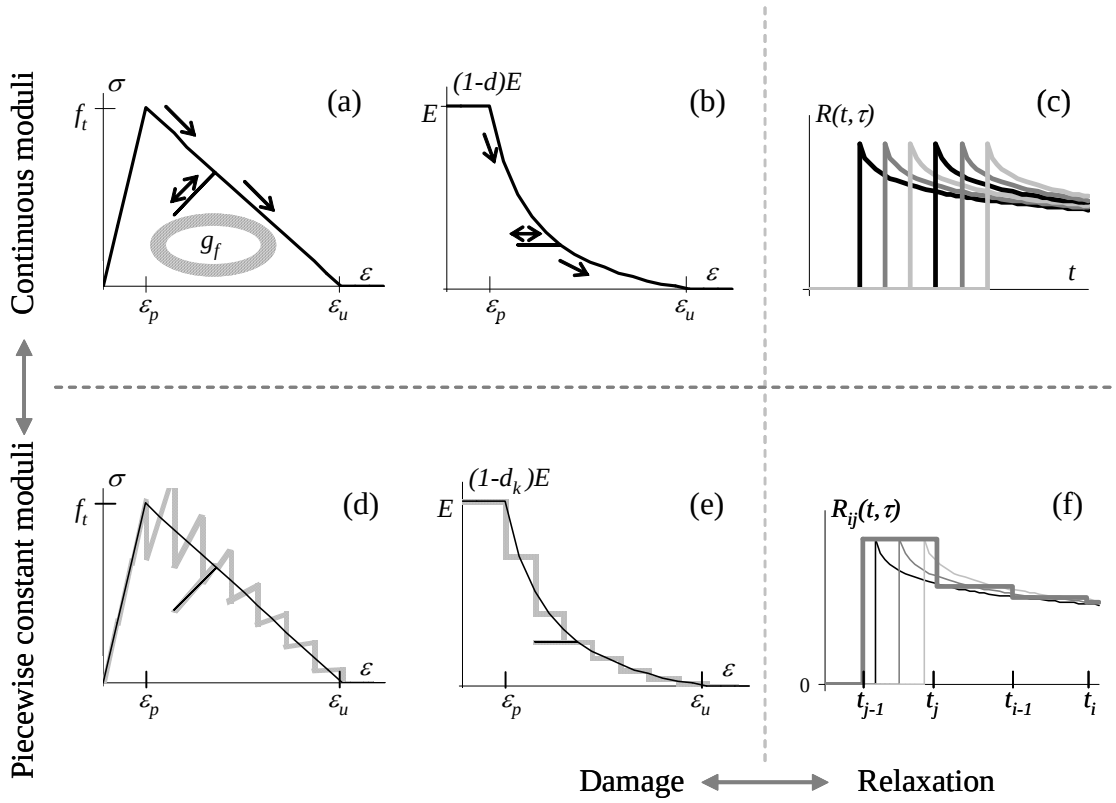

Figure 1. (a): Effect of the damage function *d* on the stress strain diagram. Temporarily unloading and reloading results in secant behavior. (b): Effect of the damage function *d* on the stiffness. Temporarily unloading and reloading results in a constant, yet reduced, stiffness. (c): Relaxation function *R* (d,e): Discretization of the damage d with respect to the maximum strain (f): Discretization of *R* with respect to time *t* and loading time τ.

The result of such a discretization is referred to as saw-tooth tension softening. Figure 1(d,e) depicts the result. For further details de reader is referred to [1].

Note that the creep model, Eq. 3, is directly based on integrating the time history in every, integration, point. For the current application the storage of the strain history is not envisioned as a drawback. Approximating the relaxation by a Dirichlet or a Taylor series is avoided.

Finally it is stressed that the failure criterion is *not* a stress criterion but a strain criterion. This is illustrated in Figure 2 for both the continuous case and the piecewise constant case. The effect of relaxation is indicated with the creep coefficient φ, Figure 2(a), a relaxation stiffness E_R and an instantaneous stiffness E_I, Figure 2(b). The relevance will be illustrated in the validation section.

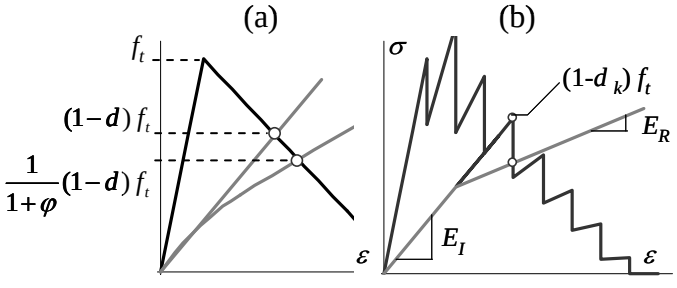

Figure 2. (a): Failure points in a stress strain diagram for an inviscid stress strain trajectory and for a stress strain trajectory including relaxation effects. (b): Similar, but now for the discretized stress strain diagram

3 NUMERICAL SOLUTION

The outline of the solution algorithm is as follows. Assume that at time t_{i-1} the damage $d(t_{i-1})$ and the strain history $\Delta\varepsilon(t_1)\ldots\Delta\varepsilon(t_{i-1})$ are known in each (integration) point and consider the time interval $[t_{i-1}, t_i]$. For this time interval, cycles of linear analyses are executed, leading to a possible increase of the damage values d_k and leading to a completion of the strain history with $\Delta\varepsilon(t_i)$. Based on the combination of two stress fields $\boldsymbol{\sigma}(\lambda) = \boldsymbol{\sigma}_R(t_i) + \lambda\boldsymbol{\sigma}_I(t_i)$, representing relaxation stresses and instantaneous stresses, a load factor λ is determined with $0 \le \lambda \le 1$. Factor λ is defined as the maximum load factor for which all integration points still satisfy the stress-strain criterion.

For the case $\lambda \neq 1$ it is not possible to apply the complete load. In this case a critical point is determined. If $\lambda = 1$ the full load has been successfully applied. The numerical procedure continues with the next time step, by passing through the new damages variables and by updating the strain history. If $\lambda < 1$ the damage level $k = k + 1$ of the critical point is incremented. The numerical procedure continues with a new cycle.

4 VALIDATION

To validate the model, the results of three-point bending tests performed by Zhou [2] are used. Figure 3(a) shows the finite element model employed for the analysis. It consists of plane-stress, four-noded quadrilateral elements. Figure 3(b,c) also show the used saw-tooth tension softening diagram and the downstairs relaxation moduli.

Figure 4 shows the results of a simulation of displacement-controlled experiments with a, relatively high, deflection rate of 5 $\mu m/s$. Next Figures 5 and 6 show the results of a simulation of two experiments with a sustained load at respectively 76% and 80% of the peak load. After the indicated points of failure in Figure 5 it is no longer possible to reach the 76% respectively 80% of the peak load, $\lambda < 1$, but the damage controlled analyses are continued.

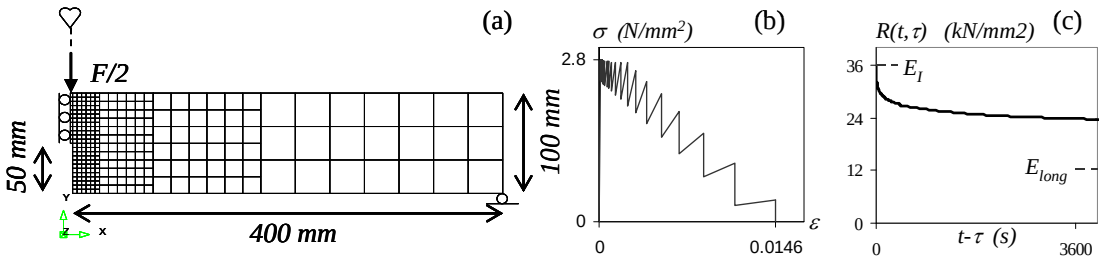

Figure 3. (a): Three-point bending tests by Zhou [2]. (b) Sawtooth tension softening diagram: stress-strain based failure envelop (c) Relaxation modulus versus time.

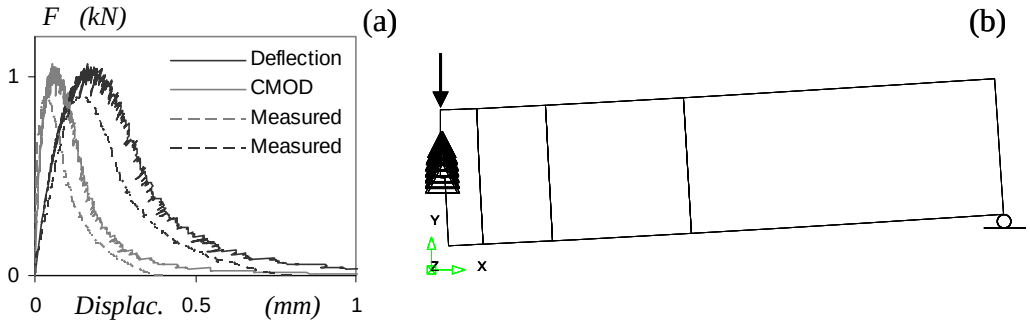

Figure 4. Three-point bending test. (a): Force-CMOD and force-deflection results, experimental [2] and numerical. (b): Displacements and damage locations.

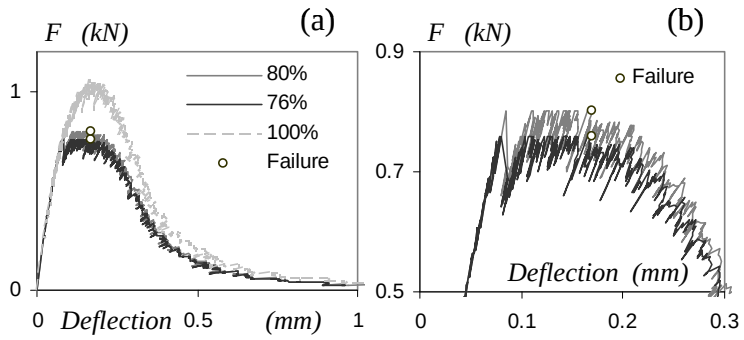

Figure 5. Three-point bending test. (a): Sustained load response at 0.76 *kN* (76%) and 0.80 *kN* (80%) and displacement controlled results. (b): Detail of (a).

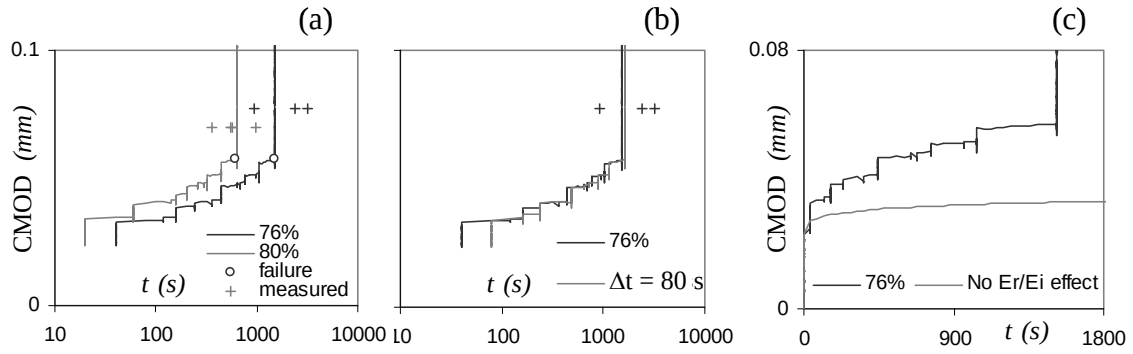

Figure 6. Three-point bending test. (a): CMOD evolutions for sustained load response at 0.76 *kN* (76%) and 0.80 *kN* (80%) (b): CMOD evolutions for sustained load response at 0.76 *kN* (76%) with Δt = 40 *s* and Δt=80 *s*. (c): CMOD evolutions for a pure tensile stress criterion "No Er/Ei effect".

Figure 6(a) shows CMOD evolutions for sustained load response at 76% and 80% of the peak load. The figure also indicates the experimental points of failure with a +-sign. The numerical analyses underestimate the CMOD values at failure; the predicted failure times are reasonable. For the case of a sustained load at 76% of the peak load, Figure 6(b) shows that the numerical results are hardly affected by increasing the time intervals Δt from 40 *s* to 80 *s*. Finally, Figure 6(c) illustrates that the use of a pure stress criterion would lead to erroneous results where failure is not reached at all.

5 CONCLUSION

The present extended abstract shows that a combined discretization of the relaxation modulus and the damage evolution, leading to a downstairs relaxation diagram and a saw-tooth tensile softening diagram, indeed allows a sequentially linear analysis for modeling creep induced failure. The main attractiveness is that the sequential linear analysis always "converges".

As a side issue the abstract dealt with the constitutive modeling of combined tensile damage and creep effects. A total strain model has been adopted which is *not* based on strain decomposition. Instead the damage has a multiplicative effect on the effective relaxation modulus. In this framework it is important to use a combined stress-strain based failure criterion rather than a pure stress based criterion.

6 REFERENCES

[1] Hendriks, M.A.N., Rots, J.G. (2008), "Simulation of creep induced cracking based on sequentially linear analysis", In: Proceedings of the 8th International Conference on Creep, Shrinkage and Durability of Concrete and Concrete Structures, Tada-aki Tanabe et al. (eds.) Ise-Shima, 579-585, volume 1.

[2] Zhou, F.P. (1992), "Time-dependent crack growth and fracture in concrete", Dissertation, Lund Univ., Lund, Sweden.

Simulation of Masonry Beams Retrofitted with Engineered Cementitious Composites

M.A. Kyriakides
Department of Civil & Environmental Engineering, Stanford University, USA
S.L. Billington
Department of Civil & Environmental Engineering, Stanford University, USA
M.A.N. Hendriks
Faculty of Civil Engineering and Geosciences, Delft University of Technology, The Netherlands

Keywords: Unreinforced masonry, engineered cementitious composites, sprayable, retrofit, non-linear finite element analysis

1 INTRODUCTION

A thin layer of ductile fiber-reinforced mortar material referred to as Engineered Cementitious Composites, or ECC has been experimentally investigated as a seismic retrofit for unreinforced masonry infill walls in non-ductile reinforced concrete frames. Compression tests of masonry prisms retrofitted with 13mm of ECC were conducted representing the compression strut of a masonry infill under in-plane lateral loading. Similarly, flexural tests of brick beams using a quarter point bending configuration with the constant moment region intended to approximately represent direct tension (in particular in the ECC), were performed to investigate the response of the tension strut of the masonry infill. In-plane cyclic tests of $1/5^{th}$ scale non-ductile concrete frames with ECC retrofitted masonry infills using different retrofit techniques were also conducted and the results indicated that the ECC can help keep unreinforced masonry walls intact to large lateral drifts, adding significant ductility to the structural system (Kyriakides & Billington, 2008). Different 2D modeling approaches using the commercial finite-element software DIANA to predict the performance of retrofitted masonry under 4-point bending are investigated and are presented here. This study supports on-going research to develop reliable methodologies for researchers and practitioners to assess the performance of non-ductile concrete unreinforced masonry infilled structures retrofitted with ECC using nonlinear finite-element analysis.

2. MASONRY BEAMS WITH UNREINFORCED AND REINFORCED ECC RETROFITS

ECC is a class of high performance fiber-reinforced cement-based composites that exhibits fine, multiple cracking and strain hardening behavior in direct tension. A sprayable version of this material was recently reported to be sprayed on to a concrete wall achieving a thickness of 45mm (Kim et al., 2003). The mix design consists of Type I Portland cement, class F fly ash, calcium aluminate cement, fine silica sand and 2% by volume of short, chopped polyvinyl alcohol fibers that have been treated with oil to allow for frictional debonding during cracking.

Flexural tests have indicated that the strength and more importantly the ductility of a retrofitted brick beam under four-point bending are increased tremendously (Figure 1). Especially when the thin layer of ECC is slightly reinforced with a steel wire mesh, more cracks are developed and propagate in the constant moment region leading to a more ductile response

(Figures 1 and 2) than when unreinforced ECC is used. On the other hand, plain brick beams demonstrated very brittle failure with approximately 20-25 times lower strength.

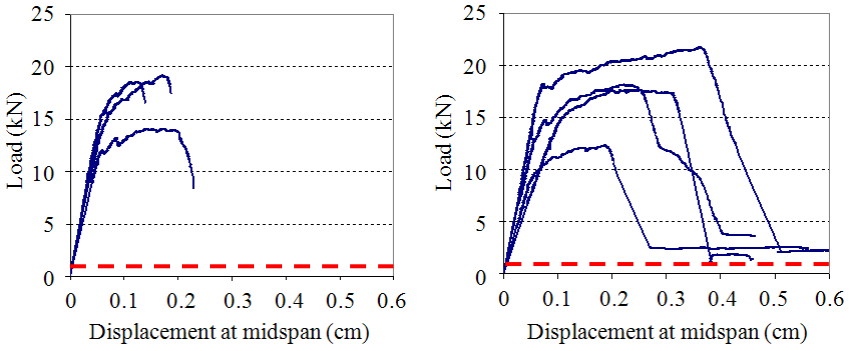

(a) (b)

Figure 1 Flexural response of masonry beams with a 13mm layer of (a) ECC, and (b) ECC with 0.125% by area steel reinforcement, troweled to the brick surface

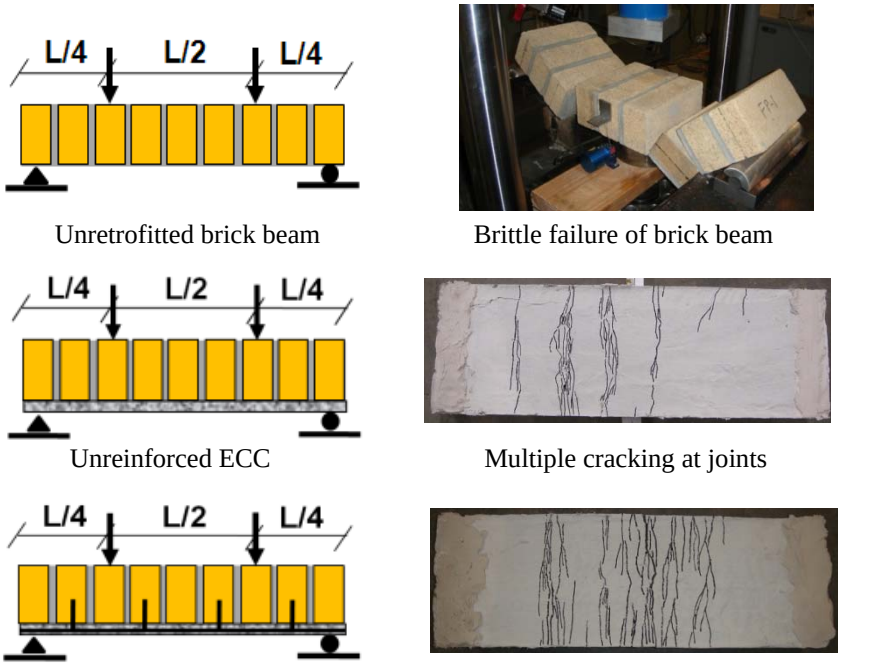

Unretrofitted brick beam — Brittle failure of brick beam

Unreinforced ECC — Multiple cracking at joints

0.125% Reinforced ECC — Multiple cracking at constant moment region

(a) (b)

Figure 2 (a) Load application and (b) cracking response of 4-point bend specimens with no retrofit (top), unreinforced ECC (center) and with ECC reinforced with 0.125% by are steel and attached to anchors (“Stitch dowels”) grouted into the masonry (bottom).

3. NUMERICAL INVESTIGATION OF RETROFITTED MASONRY

The ability to predict adequately the performance of a masonry infilled reinforced concrete structure has been a significant area of research over the last several decades in large part due to its importance for practitioners. This effort becomes more complicated when a retrofit technique is applied on the masonry infill. In this research, the ability of state-of-the-art nonlinear finite element analysis methods to predict the performance of 4-point bending masonry components retrofitted with a thin layer of ECC with and without reinforcement is being investigated.

Three different 2D finite-element modeling approaches are investigated (Figure 3). In all three approaches, 8-noded plane stress elements are used to model the brick units and a total strain, fixed crack model (Feenstra et al., 1998) is used to capture the brick cracking behavior.

Plane stress elements are also used to model the ECC layer areas directly below the brick units, with a multi-linear (in tension) crack model (also total strain, fixed crack). To simulate the bond between the ECC layer and the brick units, linear elastic interface elements are used. The primary difference of the three modeling approaches is found in the way the mortar joints and the ECC layer directly below the mortar joints is modeled. In the first model, continuum elements are used for the mortar joints and the ECC below, with interface elements introduced between the brick units and the mortar to capture the brick-mortar interface failure (Figure 3a). In the second approach, interface elements are used for the entire mortar joint and the ECC below the mortar joint (Figure 3b). With the third approach, "blown-up" brick units and zero thickness interface elements for mortar joints and the ECC directly below are used (Figure 3c).

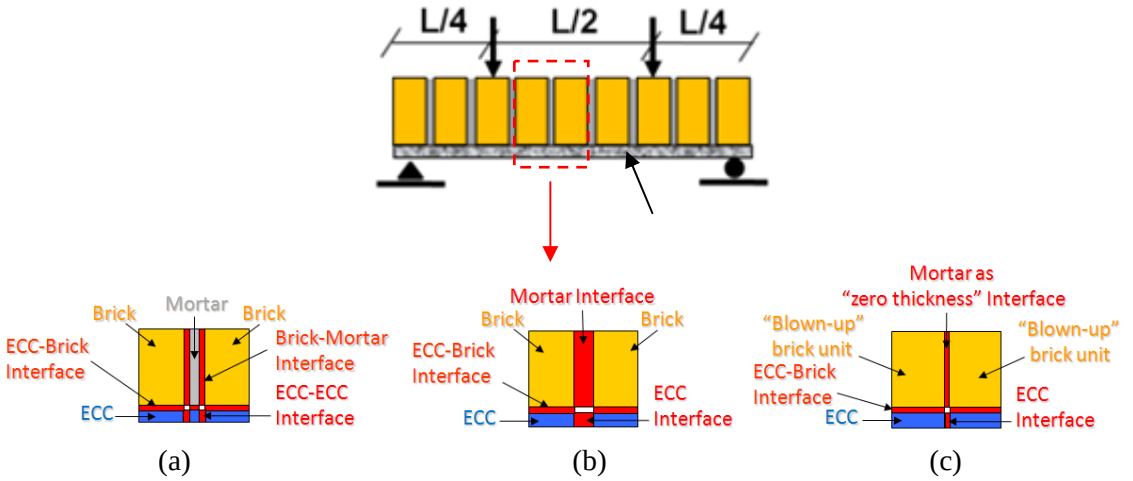

(a) (b) (c)

Figure 3 Schematic representation of the three modeling approaches (a) Continuum elements for mortar joints and ECC with interface elements between the brick and the mortar, (b) interface elements for the mortar joints and the ECC directly below, and (c) blown-up brick units with zero thickness mortar joints.

The first and the third modeling approaches were able to capture adequately the experimental responses of both the unreinforced and reinforced ECC retrofitted brick beams in terms of strength, ductility and failure mode. In both of these models, failure of the mortar-brick interfaces at the constant moment region occurred first, followed by cracking of the ECC under the mortar joints that led to a stiffness degradation of the beam, and eventually failure of the ECC below the 3rd mortar joint (in the constant moment region) (Figure 4). In all analyses, a higher initial stiffness was obtained compared to the experiments (Figure 5). Especially with the second approach, the analytical stiffness was even higher compared to that predicted by the other models, as the second model does not satisfy the moment equilibrium due to the finite thickness of the mortar joints. While the first and third modeling approaches gave a similar load vs. displacement response, the third approach is a less complicated in terms of developing the model and is considered preferable for evaluation of larger-scale, structural simulations.

REFERENCES

[1] Feenstra, PH, Rots, JG, Arnesen A, Teigen, JG, and KV Hoiseth (1998) "A 3D constitutive model for concrete based on a con-rotational concept," *Computational Modelling of Concrete Structures, Proc. of EURO-C 1998*, de Borst, Bicanic, Mang & Meschke (eds), Balkema, Rotterdam, p. 13-22.

[2] Kim, YY, Kong, HJ, and VC Li (2003), "Design of Engineered Cementitious Composite (ECC) Suitable for Wet-Mixture Shotcreting." *ACI Materials J.*, **100**(6):511-518.

[3] Kyriakides, MA, and SL Billington (2008) "Seismic Retrofit of Masonry-Infilled non-ductile Reinforced Concrete Frames using Sprayable ECC," *Proceedings of the 14th World Conference on Earthquake Engineering* (14WCEE), Beijing, China, October.

[4] Rots, JG (1997) "Structural Masonry. An Experimental /Numerical Basis for Practical Design Rules." TNO Building and Construction Research, Rijswijk, Netherlands.

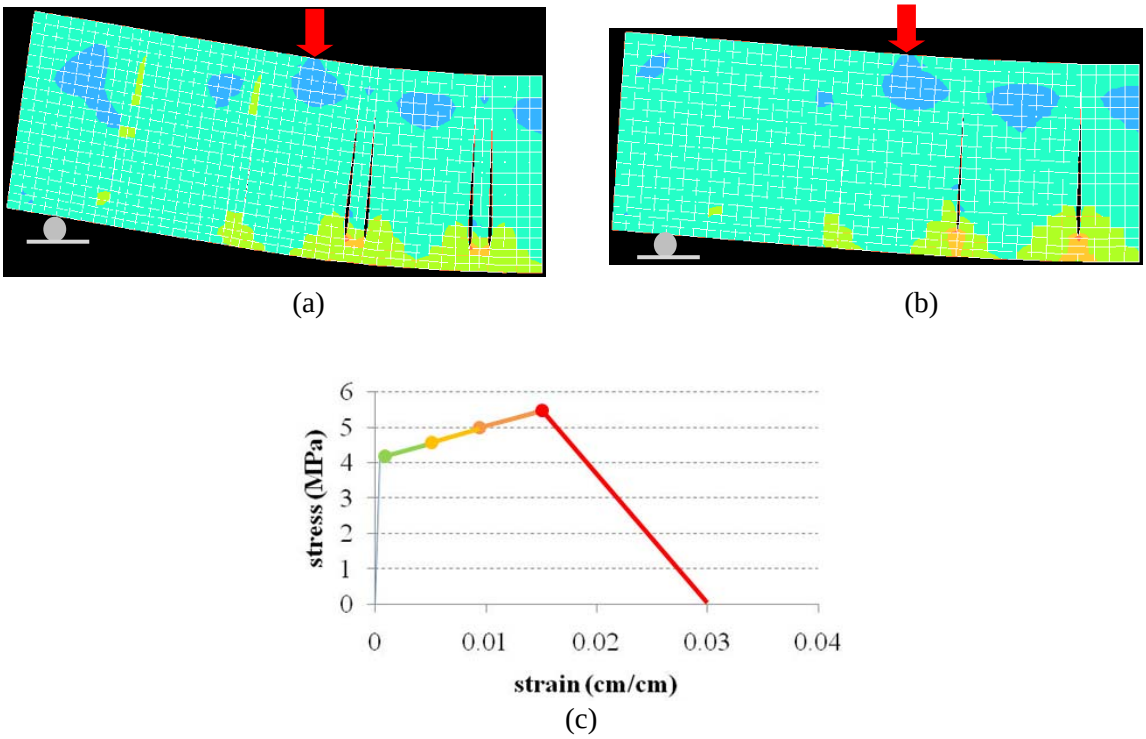

Figure 4 Principal tensile stresses of half brick beam with ECC at failure using (a) Continuum elements for mortar joints and ECC with interface elements between the brick and the mortar and (b) blown-up brick units with zero thickness interface elements for mortar joints during failure of the ECC. Diagram (c) shows the tensile stress-strain response of the ECC with colors that correspond to the tensile strains shown in (a) and (b).

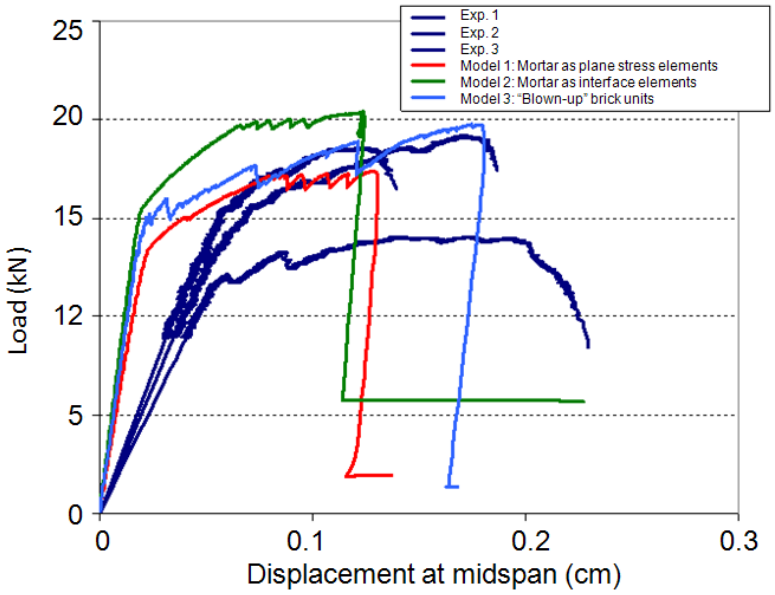

Figure 5 Load-displacement responses obtained from both experiments and all three model approaches.

Recent advances in masonry homogenization

P.B. Lourenço
ISISE, University of Minho, Portugal

G. Milani
Politecnico di Milano, Italy

A. Zucchini
ENEA, Italy

Keywords: Micro-mechanics, limit analysis, orthotropic failure envelop, validation

1 INTRODUCTION

Homogenization remains a popular subject in masonry research. Usually the complex geometry of the basic cell is replaced by a simplified geometry so that a close-form solution of the homogenization problem is possible. Many other approaches involving different approximations and ingenious assumptions have been sought. To overcome the weak approximation, a micro-mechanical homogenization model that consider additional internal deformation mechanisms and a model based on the polynomial expansion of the stress field inside the R.V.E. are presented.

2 A MICRO-MECHANICAL HOMOGENIZATION APPROACH

As a consequence of the differences in stiffness between units and mortar, a complex interaction between the two masonry components occurs when masonry is deformed. The differences in stiffness cause an unequal distribution of deformations over units and mortar, compared with the average deformation of masonry composite. As a result the individual (internal) stresses of units and mortar deviate from the average (external) stresses of the composite. The elastic mechanical properties of an orthotropic material equivalent to a basic masonry cell can be derived from a suitable micromechanical model with appropriate deformation mechanisms, which take into account the staggered alignment of the units in a masonry wall. The unknown internal stresses and strains can be found from equilibrium equations at the interfaces between the basic cell components, from a few ingenious assumptions on the kinematics of the basic cell deformation and by forcing the macro-deformations of the model and of the homogeneous material to contain the same strain energy. This homogenisation model has been extended, by coupling the elastic micro-mechanical model with a damage model for joints and units by means of an iterative solution procedure to calculate the damage coefficients. A simple isotropic damage model with only one single parameter has been utilized, because the discrete internal structure of the cell, and implicitly its global anisotropic behaviour, is taken into account by the three-dimensional micromechanical model.

When the basic cell is loaded only with normal stresses, the micromechanical model assumes that all shear stresses and strains inside the basic cell can be neglected, except the in-plane shear stress and strain (σ_{xy} and ε_{xy}) in the bed joint and in the unit. The non-zero stresses and strains in the bed joint, head joint and unit are assumed to be constant, with the exception of the normal stress σ_{xx} in the unit, which is a linear function of x and accounts for the effect of the shear σ_{xy} in the bed joint, and with the exception of the shear stress σ_{xy} in the unit, which is linear in y. The coupling of this model with non-linear constitutive models, leads to an iterative algorithm,

in which at each cycle a system of equilibrium equations is solved to obtain the unknown effective stresses and strains.

The model was applied to a real masonry basic cell and compared with the results of an accurate finite element analysis (FEA) under linear elastic analysis. In the finite element analysis and the analytical model, the properties of the components can be taken absolutely equal. Different stiffness ratios between mortar and unit are considered. The material properties of the unit are kept constant, whereas the properties of the mortar are varied to yield a ratio E_b / E_m ranging from 1 to 1000. The adopted range is very large, if only linear elastic behaviour of mortar is considered. However, those high values are indeed encountered if inelastic behaviour is included. In such case, E_b and E_m should be understood as linearised tangent Young's moduli, representing a measure of the degradation of the (tangent / secant) stiffness matrices utilised in the numerical procedures adopted to solve the non-linear problem. Note that the ratio E_b / E_m tends to infinity when softening of the mortar is complete and only the unit remains structurally active. The elastic properties of the homogenised material, calculated by means of the proposed micro-mechanical model, are compared in Figure 1a with the values obtained by FE analysis. The agreement is very good in the entire range $1 \leq E_b / E_m \leq 1000$, with a maximum error ≤ 6%. A comparison between the results obtained with the micro-mechanical model and experimental results is given in Figure 1b. Very good agreement is found in the shape of the yield surface, indicating that the proposed model can be used as a possible macro-model to represent the composite failure of masonry.

Figure 2 shows the validation of the model under non-linear uniaxial loading. The algorithm has been tested in the fracture problem of an infinitely long wall under tensile loading parallel to the bed joint (Figure 2a). The model reproduces with good agreement the FE analysis of the cell degradation and the two peaks of the failure load for a zero dilatancy angle in the joints. The head joint is the first to fail in tension and the bed joint takes its place in the load carrying mechanism of the cell. The load is transferred through bed joint shear from unit to the other, with the cell showing regained elastic behaviour for increasing loads, until final failure of the bed joint in shear. The residual load carrying capacity is zero because there is no vertical compression, and therefore no friction effect.

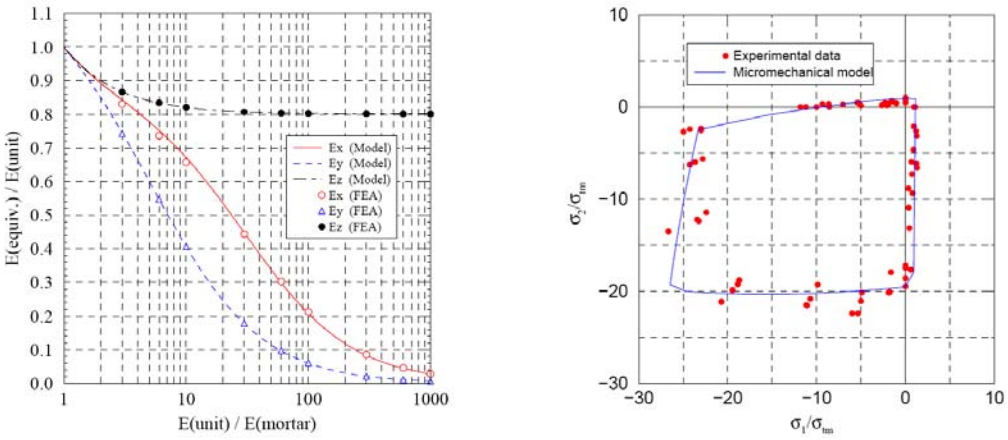

(a) (b)

Figure 1. Elastic results for the micro-mechanical model: (a) comparison of Young's moduli with FEA results for different stiffness ratios; (b) comparison with experimental results of Page (1981,1983).

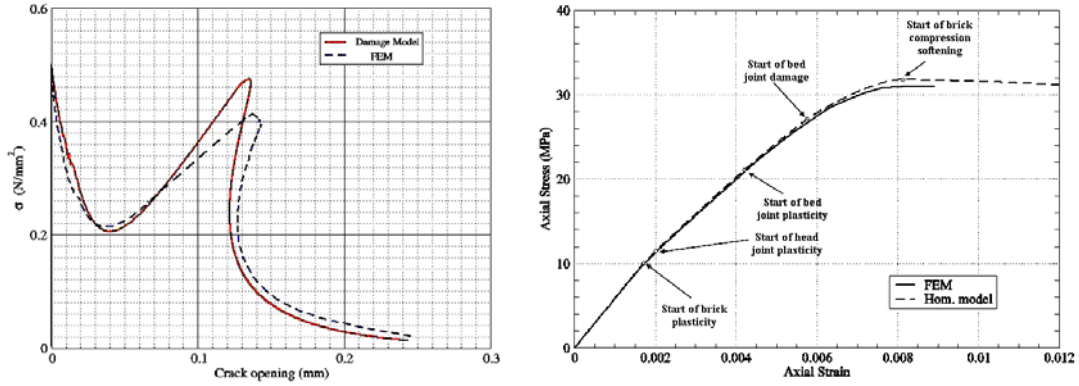

(a) (b)

Figure 2. Inelastic response of the model: (a) post-peak tensile behaviour and comparison with FEM results; (b) axial stress vs. axial strain and comparison between finite element simulation.

Figure 2b shows the behaviour of a basic masonry cell under axial compressive loading perpendicular to the bed joint and a comparison with an accurate FE calculation. The curves obtained with the homogenisation model almost coincide with the corresponding FE results, with marginal computational effort and no convergence difficulties. For weak mortars the plastic flow of the mortar joints starts very early in the loading path, while the brick non-linear behaviour begins a little later. The brick is in a tension-compression-tension state, while the mortar is in a tri-axial compression state for the lateral containment effect of the stiffer brick. The head joint suffers some negligible damage in tension just before the complete failure of the brick in tension, which leads to the catastrophic failure of the entire cell. For strong mortars the plastic flow starts earlier in the brick than in the bed joint, due to the higher strength of the mortar. The inversion of the elastic mismatch between mortar and brick in this case (the mortar is much stiffer than the brick) yields in this case a tension-tension-compression state of the bed joint. A substantial (57%) isotropic damage in tension is reached in the bed joint, but the failure of the masonry cell is driven again by the crushing of the brick. The damage of the mortar in the bed is due to the high tension in the *x* and *z* direction.

3 A STRESS FIELD EXPANSION APPROACH

Using the lower bound theorem of limit analysis and the hypotheses of homogenization, a solution for the homogenization problem can be derived by means of a (non-linear) optimization problem. Here, the masonry cell is sub-divided into thirty-six sub-domains and, for each sub-domain, polynomial distributions of cubic degree are assumed for the stress components.

In Figure 3a,b the principal stress distribution at collapse from the lower bound analysis and the velocities at collapse from the upper bound analysis are reported. Good agreement is found among the model here proposed and experimental data. Finally, in Figure 3c a comparison between the numerical failure loads provided respectively by the lower and upper bound approaches and the experimental load-displacement diagram is reported. Collapse loads P(–) = 210 kN and P(+) = 245kN are numerically found using a model with 288 triangular elements, whereas the experimental fail-ure shear load is approximately P = 250 kN.

The homogenized model is also employed in order to reproduce experimental data for panels out-of-plane loaded. Figure 4a shows typical comparisons between experimental pressure-displacement curves, numerical pressure-displacement curves obtained by means of an orthotropic elasto-plastic macro-model and the results with the proposed formulation. Figure 4b shows results of the numerical analysis in terms of ultimate principal moment distribution and failure mechanisms. The agreement with experimental results is worth noting in all cases analysed. Finally, some real scale application of the model to a building in Italy is shown in Figure 4c, demonstrating the possibility of using the proposed tools for safety evaluation. In this case, a complex collapse mechanism involving piers and walls has been found.

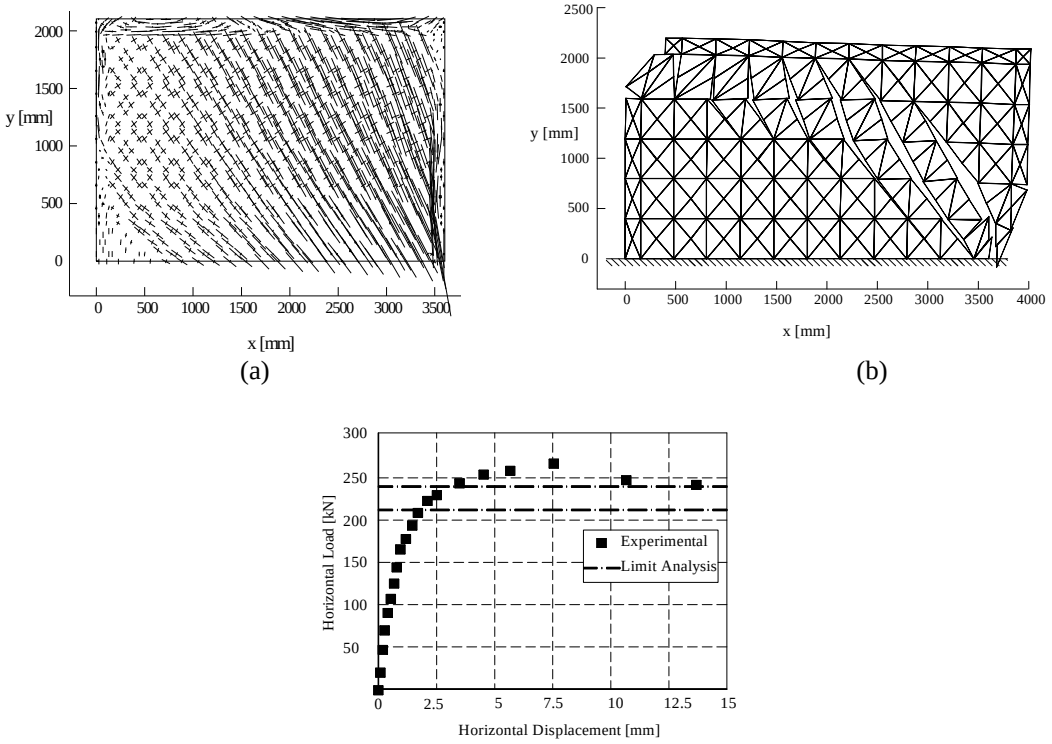

Figure 3. Shear wall:. (a) Principal stress distribution at collapse, lower bound; (b) Velocities at collapse, upper bound; (c) Comparison between experimental load-displacement diagram and limit analysis.

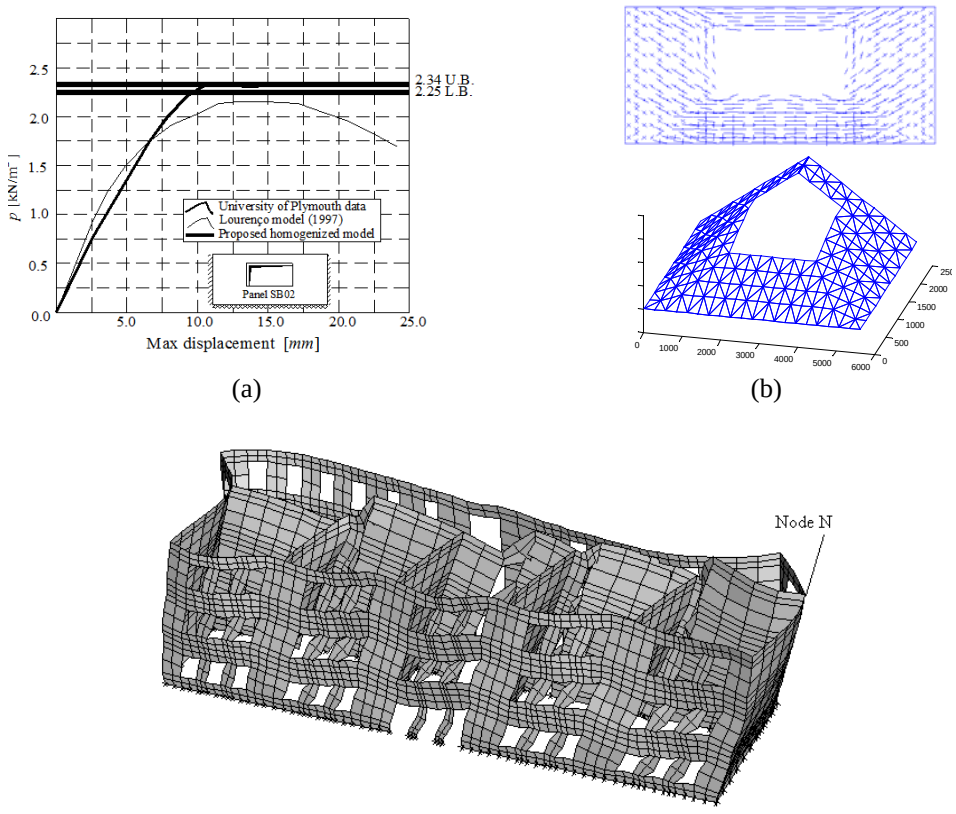

Figure 4. Results involving out-of-plane loading: (a) comparison between experimental and numerical results for masonry wall subjected to out-of-plane loading; (b) lower (principal moments at collapse) and upper bound results (deformed mesh at collapse and yield line pattern) for the same wall; (c) collapse of a masonry building subjected to earthquake action.

4 RELATED PAPERS

Overview

[1] Lourenço, P.B., Milani, G., Tralli, A., Zucchini, A., Analysis of masonry structures: review of and recent trends of homogenisation techniques, *Canadian Journal of Civil Engineering*, 34 (11), p. 1443-1457 (2007)

Micro-mechanical model

[2] Zucchini, A., Lourenço, P.B., Mechanics of masonry in compression: Results from a homogenisation approach, *Computers & Structures*, 85(3-4), p. 193-204 (2007)

[3] Zucchini, A., Lourenço, P.B., A coupled homogenisation-damage model for masonry cracking, *Computers & Structures*, 82, p. 917-929 (2004)

[4] Zucchini, A., Lourenço, P.B., A micromechanical model for the homogenisation of masonry, *Int. J. Solids and Structures*, 39(12), p. 3233-3255 (2002)

Finite element limit analysis

[5] Milani, G., Lourenço, P.B., Blast analysis of enclosure masonry walls using homogenization approaches, *International Journal for Multiscale Computational Engineering* (accepted for publication) (January, 2009)

[6] Milani, G., Lourenço, P.B., A simple discontinuous upper bound limit analysis approach with sequential linear programming mesh adaptation, *International Journal of Mechanical Sciences*, 51(1), p. 89-104 (2009)

[7] Milani, G., Lourenço, P.B., Tralli, A., 3D Homogenized limit analysis of masonry buildings under horizontal loads, *Engineering Structures*, 29(11), p. 3134-3148 (2007)

[8] Milani, G., Lourenço, P.B., Tralli, A., A homogenization approach for the limit analysis of out-of-plane loaded masonry walls, *J. Struct. Engrg., ASCE*, p. 1650-1663 (2006)

[9] Milani, G., Lourenço, P.B., Tralli, A., Homogenised limit analysis of masonry walls. Part I: Failure surfaces, *Computers & Structures*, 84(3-4), p. 166-180 (2006)

[10] Milani, G., Lourenço, P.B., Tralli, A., Homogenised limit analysis of masonry walls. Part II: Structural applications, *Computers & Structures*, 84(3-4), p. 181-195 (2006)

Simulation of complex failure mechanisms in composite laminates with the phantom node method and a dissipation based arclength method

F.P. van der Meer
Delft University of Technology, Faculty of Civil Engineering and Geosciences

L.J. Sluys
Delft University of Technology, Faculty of Civil Engineering and Geosciences

Keywords: fiber reinforced composites, phantom node method, arclength methods, failure

INTRODUCTION

Failure in composite laminates can be constituted of different micromechanical processes. The need to have each of these represented properly makes simulation of failure in laminates a challenging task. At the same time, the fact that these different processes may occur contributes to the importance of numerical simulation, because it disqualifies conventional mechanical methods for the prediction of the ultimate strength. One can think of the size effects in notched laminates observed by Green et al. [1]. It was reported that (i) increasing the ply thickness promotes failure mechanisms in which delamination dominates, and that (ii) upon in-plane scaling the normalized strength of a notched laminate increases when delamination drives the failure while it decreases when failure of the fibers is dominating the response. These trends can be understood qualitatively, but advanced models are needed to capture them numerically.

In this paper, a short overview is presented of a finite element framework in which separate models for splitting, delamination and fiber failure are combined. Together, the different models allow for a kinematically correct representation of complex laminate failure mechanisms, which is a first prerequisite for reliable failure simulation and prediction. Constitutive laws in the different models are kept as simple as possible without losing sight of the actual physical processes. Furthermore, a carefully designed loading strategy is adopted to follow the quasi-static equilibrium path through different failure events.

FAILURE MODELS

In the present framework, laminates are modeled on the mesolevel, i.e. each ply is modeled separately with a layer of solid elements. The presented results are obtained in plane stress analyses; each of the plies is represented with plane stress elements.

The phantom node method [2] is applied to model intraply matrix cracking. With this method, cracks are represented as mesh-independent discontinuities in the displacement field. In our implementation, the direction of crack propagation is set equal to the fiber direction, such that typical matrix crack patterns are obtained. Cracks are allowed to initiate anywhere along the boundary or in the interior of the specimen if the local stress exceeds the matrix failure criterion. The only restriction for crack initiation is a minimum crack spacing; the projected distance between two cracks in the same ply has to be at least such that multiple cracking inside a single element is avoided. For details on the model for matrix cracking, we refer to [3].

Delamination is modeled with interface elements. As a consequence of the plane stress approach, the only delamination mode that is captured is shear delamination, which we consider an acceptable simplification for preliminary analysis of cases with in-plane loading conditions.

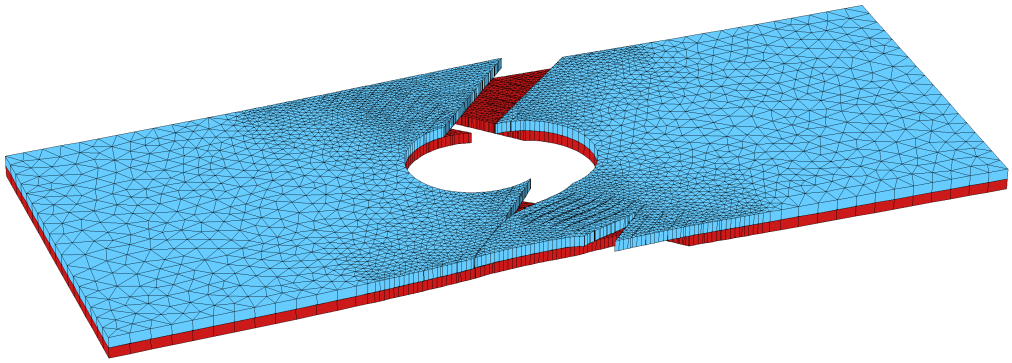

Figure1. Open hole tension: deformed mesh short before final failure.

A bilinear damage law relates the interface traction to the ply separation, where, in contrast with common practice for interface elements, the initial stiffness is not merely a numerical parameter, since it can be related to elastic out of plane shear deformation of the plies.

Concerning the interaction between matrix cracking and delamination, interface elements are not adapted when the kinematics of the connected elements change due to the presence of matrix cracks. For this, it is particularly advantageous that, in the phantom node method, unknowns that represent the nodal displacements of the uncracked element, remain one-to-one related to the displacement of the material point at the node. The error due to not updating the kinematics of the interface elements vanishes upon mesh refinement and has been found to be very small for reasonable element sizes, particularly when a nodal integration scheme is used [4].

Fiber failure is represented with a continuum damage model. The damage model is orthotropic in the sense that it is governed by the strain in fiber direction. The effect of damage, however, is isotropic stiffness degradation, reflecting the fact that the process in which fibers fail does not leave the matrix intact either.

LOADING STRATEGY

When matrix cracking and delamination occur in fiber reinforced laminates, two processes take place simultaneously: matrix material damages, and fibers unload. Because the fibers are very stiff and the matrix failure process is not very ductile, the amount of elastic energy released by the second process easily exceeds the amount of energy necessary to drive the first. Hence, unstable crack propagation occurs, and snapback behavior is observed when the equilibrium path is followed.

The dissipation based arclength method [5] is very useful to perform such analyses with sharp snapbacks. It is similar to classical arc-length methods in the sense that the loadscale in each time step is treated as an unknown and a constraint equation is added to the system of equations. In this method, the constraint equation is formulated such that the equilibrium equations are solved for a solution in which a prescribed positive amount of energy is dissipated globally. This constraint equation follows from fundamental thermodynamics and its formulation does not require any knowledge on the location of failure. In a geometrically linear context with material models that ensure secant unloading, the constraint equation can be evaluated with negligible extra computational effort. In the context of laminates, where initial stresses are present due to the mismatch in thermal expansion coefficients, an additional vector assembly over all elements has to be performed once each time step.

Furthermore, an adaptive strategy is used, firstly in the sense that the prescribed dissipation increment is adapted during the analysis, and secondly in the sense that in those phases of the analysis where no material is damaging, standard displacement control is used instead of arc-length control.

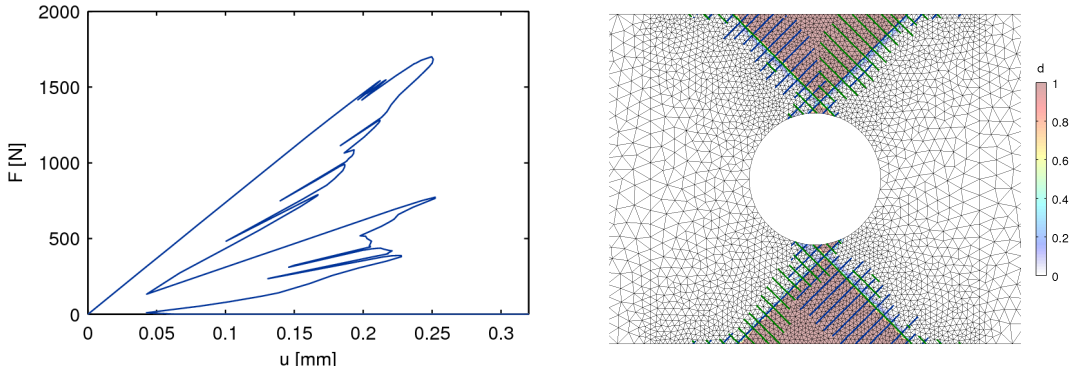

Figure 2. Open hole tension: global response (left) and final delamination and matrix cracks (right).

RESULTS

Results are presented for two cases, both dealing with a $[\pm 45]_s$ laminate. The first analysis, an open hole tension test involving only matrix cracking and delamination, illustrates the capability of the framework to analyze cases with multiple cracks and a series of sharp snapbacks. The second analysis, a compact tension test, is performed with two different values for the ply thickness and shows that particular size effects as mentioned in the introduction can be captured.

Figure 1 shows the deformed mesh from the open hole tension test in a late stage of the analysis. A number of straight matrix cracks can be observed as well as the delamination, which is complete on one side of the hole. The corresponding load-displacement diagram is shown in Figure 2. Sharp snapback events are recorded when delamination and matrix cracks allow a fiber bundle to unload. Neglecting dynamical effects for these events is not most realistic. However, the dissipation based arclength method is a powerful technique to model such dynamic events in a robust and clean manner. Following the equilibrium path gives a lower bound for the amount of damage that will be effected during the dynamic event. Furthermore, Figure 2 depicts the final delamination damage and matrix crack pattern.

The geometry for the compact tension analysis is shown in Figure 3, along with the normalized load-displacement response for two different values of the ply thickness. It can be observed that the global response for the thin ply case is more or less what one would expect for a compact tension test, while for the thick ply case, sudden catastrophic failure is predicted. This reflects a difference in failure mechanism: fiber failure dominated for thin plies and delamination dominated for thick plies.

Deformed meshes of +45° and -45° plies are shown separately in Figure 4 along with a picture with the delamination damage and matrix cracks. The difference in failure mechanism can clearly be observed. In the case with thin plies, both plies fail in a conforming sawtooth crack with alternating matrix cracking and fiber failure. In the thick ply case, there is a single dominant matrix crack in each of the two plies, and delamination in the area between those.

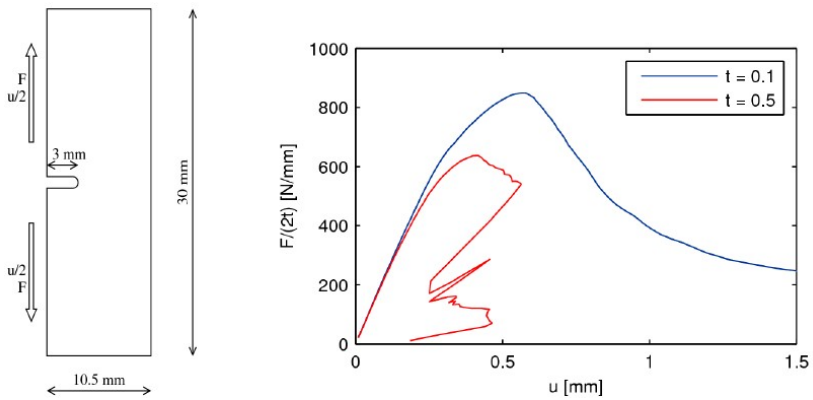

Figure 3. Compact tension: geometry and global response.

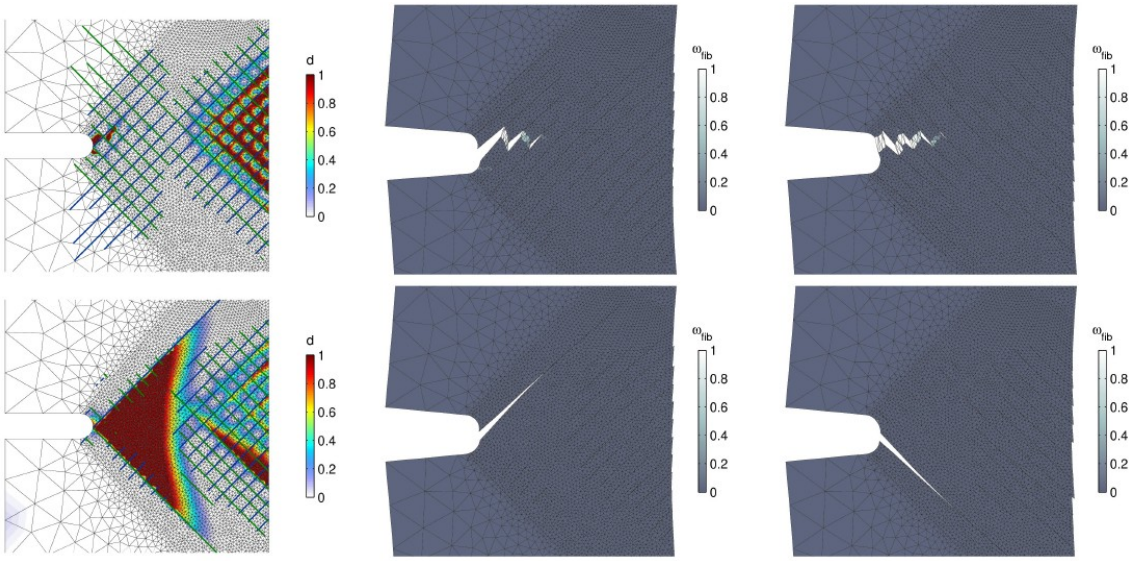

Figure 4. Compact tension: Interface damage and matrix cracking (left) and deformed meshes with fiber damage (middle, right) for compact tension test with thin plies (top) and thick plies (bottom).

DISCUSSION

A finite element framework has been developed for analysis of failure in composite laminates. The framework is comprised of the phantom node method for matrix cracking, interface elements for delamination and continuum damage for fiber failure, in combination with the dissipation based arclength method.

Robust analysis of a sequence of failure events is possible with the presented framework. Complex failure mechanisms in which different micromechanical processes interact can be described well, which allows for the prediction of specific size effects that have been observed experimentally with respect to laminate failure.

REFERENCES

[1] B.G. Green, M.R. Wisnom, S.R. Hallett, An experimental investigation into the tensile strength scaling of notched composites. *Compos. Part A*, **38**, 867-878, 2007.

[2] J.-H. Song, P.M.A. Areias, T. Belytschko, A method for dynamic crack and shear band propagation with phantom nodes. *Int. J. Numer. Meth. Eng.*, **67**, 868-893, 2006.

[3] F.P. van der Meer, L.J. Sluys, A phantom node formulation with mixed mode cohesive law for splitting in laminates. *Int. J. Fract.*, in press. Doi:10.1007/s10704- 009-9344-5.

[4] F.P. van der Meer, L.J. Sluys, Mesh-independent modeling of both distributed and discrete matrix cracking in interaction with delamination in composites. *Eng. Fract. Mech.*, submitted.

[5] C.V. Verhoosel, J.J.C. Remmers, M.A. Gutiérrez, A dissipation-based arc-length method for robust simulation of brittle and ductile failure. *Int. J. Numer. Meth. Eng.*, **77**, 1290-1321, 2009.

Comparison of two novel approaches to model fibre reinforced concrete

F.K.F. Radtke*, A. Simone* and L.J. Sluys*

*Faculty of Civil Engineering and Geosciences
Delft University of Technology
Stevinweg 1, 2628 CN Delft, The Netherlands
e-mail: f.k.f.radtke@tudelft.nl, www.mechanics.citg.tudelft.nl

Key words: Fibre Reinforced Concrete, PUFEM, Computational Modelling.

Summary. We present two approaches to model fibre reinforced concrete. In both approaches, discrete fibre distributions and the behaviour of the fibre-matrix interface are explicitly considered. One approach employs the reaction forces from fibre to matrix while the other is based on the partition of unity finite element method. In none of the methods the fibres are meshed.

1 INTRODUCTION

Fibre reinforced concrete has been applied increasingly during the last years. By adding fibres to a cementitious matrix its mechanical behaviour can be changed from brittle to ductile and the crack pattern from localised to distributed. A well-known example of fibre reinforced cementitious composites (FRCCs) are the engineered cementitious composites (ECCs) developed by Li et al.[1].

In this contribution we compare two novel computational approaches to model FRCCs. They are able to represent the link between the micro-structure of the material and its mechanical properties. We are especially interested in capturing the interaction between a fibre distribution in a specimen and its mechanical behaviour. Furthermore, we want to keep the models computationally efficient. To study the influence of varying fibre distributions, we treat the fibres in a discrete way. For the sake of computational efficiency we do not discretize the fibres but we superimpose them on a background mesh, independent of the fibre distribution as shown in Figure 1.

In the first approach fibres are represented by adding forces around fibre endpoints (fibre force approach). In the second approach a partition of unity based finite element[2,3] is developed that can incorporate discrete fibres and slip between fibre and matrix (pufem fibre approach). This enables us to study the bond behaviour in more detail than in the first approach. Both methods allow to model the influence of discrete fibre distributions on the mechanical behaviour of the material.

For convenience, we employ in both approaches an isotropic damage model with exponential softening to represent the cracking in the matrix material. For regularisation purposes different techniques like fracture energy regularisation[4], integral[5] and gradient[6] damage models are used.

2 FIBRE FORCE APPROACH

In the fibre force approach the fibres are not directly modelled. They are represented by their reaction forces to the matrix. These reaction forces P are assumed to be equal to forces measured during fibre pull-out experiments as a function of the pull-out distance Δ. If a fibre bridges a crack, a pull-out distance is derived from the crack opening and the pull-out forces are applied to the matrix. In the top part of Figure 2 a tension test studied in this example is shown. A sample with a weak part in the middle and fibre bridging this area is fixed on the left side and pulled on the right side. Two different fibre pull-out relations are employed (see left part of Figure 2). $p-\Delta\,1$ represents a hooked ended steel fibre and $p-\Delta\,2$ a straight fibre. In the right part of the figure, the

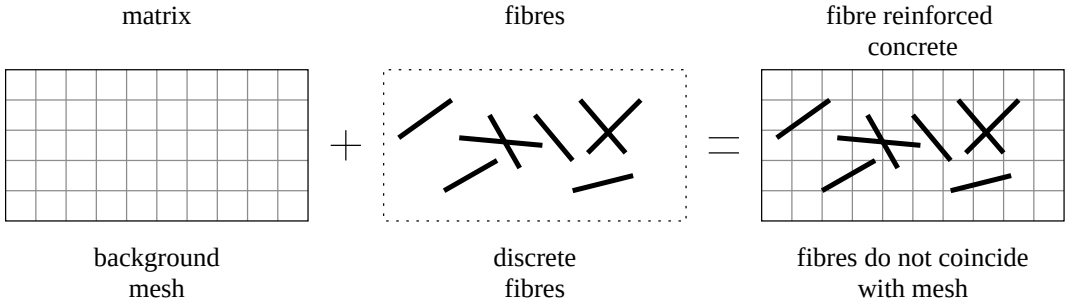

Figure 1: Discrete fibres superimposed to a background mesh to model fibre reinforced concrete.

response of the specimen is shown. The sample without fibre behaves more brittle than the fibre samples where the contribution of the pull-out forces becomes clearly visible.

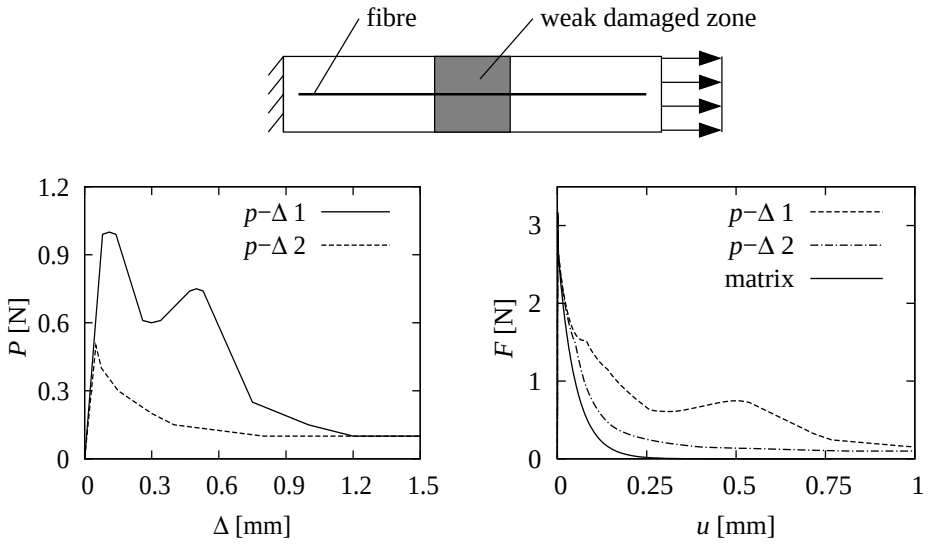

Figure 2: Use of two different fibre pull-out relations in simple tension test.

3 PUFEM FIBRE APPROACH

In the pufem fibre approach, we assume that the displacement field is enhanced by information at the fibre-matrix interface representing fibre debonding or a tunnelling crack. Furthermore, fibres used in fibre reinforced concrete are mostly thin and short. Thus, we assume that the thickness of the fibre can be neglected. Using an enrichment function which is equal to one at the fibre and zero elsewhere leads to a formulation that allows for the inclusion of an arbitrary number of arbitrarily distributed and oriented fibres in an element.

A tension test is performed on a matrix sample including horizontal fibres and two arbitrary distributions containing each nine fibres. System and results are depicted in Figure 3. Fibre, matrix and fibre-matrix interface are assumed to behave according to small strain linear elasticity. The results show the increase of stiffness when fibres are added to the matrix material.

In the second pufem fibre example (see Figure 4) we present an example based on the setup shown in Figure 2 using a simple quadratic bond law for the fibre-matrix interface. When the sample is loaded in tension, the weak part is damaged and softening starts. The results given in

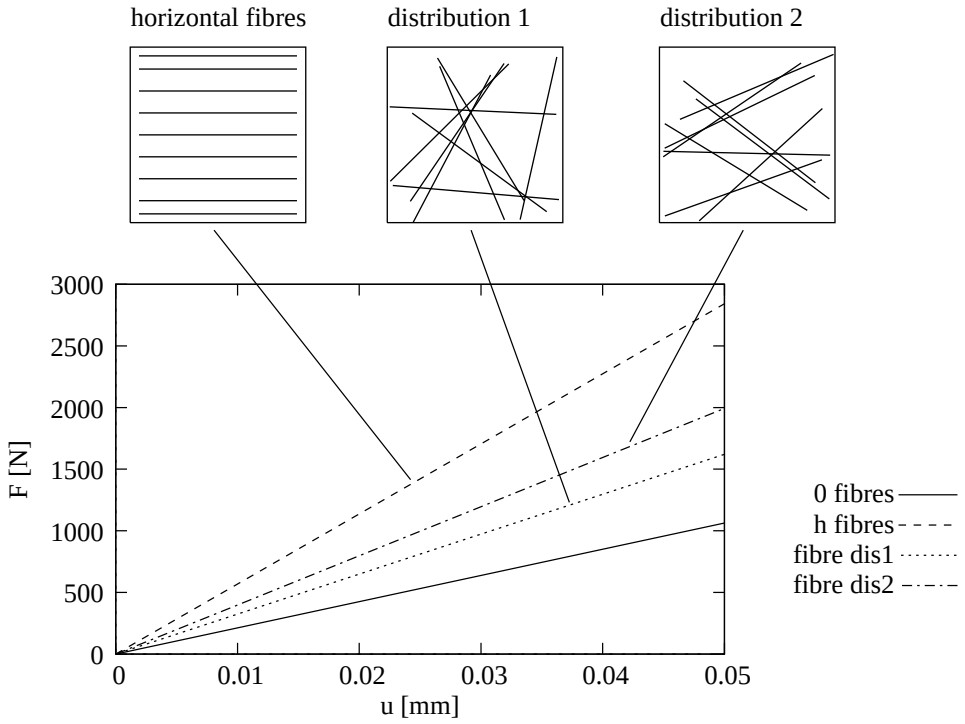

Figure 3: Comparison of three different fibre distributions.

Figure 4 show first an increase in ductility due to the fibre being pulled out of the matrix, followed by softening of the fibre-matrix bond with eventual loss of load carrying capacity.

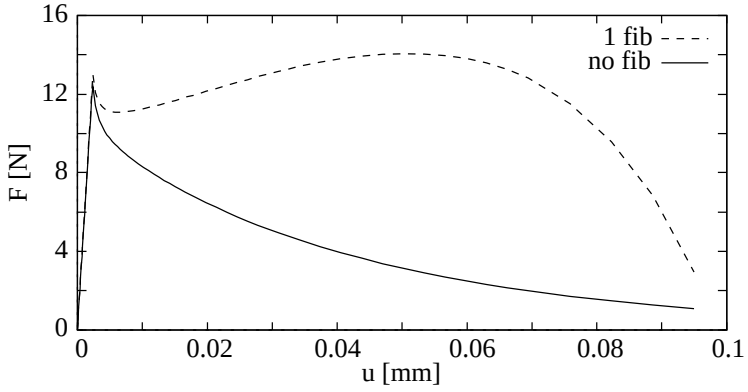

Figure 4: A simple tension test with a fibre bridging a weak part of a specimen.

4 COMPARISON AND CONCLUSIONS

We have presented two methods that are able to describe discrete fibres in a continuum matrix without meshing them which decreases the computational effort greatly. Both methods can capture the mechanical behaviour of fibre reinforced concrete. While in the fibre force approach fibres are taken into account only by the reaction forces from the fibres to the matrix, in the pufem fibre approach the fibres, the bond and the matrix material are independently modelled. Another advantage of the pufem fibre approach is that the slip between matrix and fibres is directly com-

puted and the tractions are distributed along the fibre and not applied as fibre forces around the fibre endpoints only. Although the pufem fibre approach is physically more appealing, it is also computationally more expensive; indeed, unlike the fibre force approach, each fibre introduces extra degrees of freedom.

References

[1] V.C. Li. On Engineered Cementitious Composites (ECC), A Review of the Material and Its Applications. *J. Adv. Concr. Technol.*, **1**, 215–230, (2003).

[2] J.M. Melenk, I. Babuška. The Partition of Unity Finite Element Method: Basic Theory and Applications. *Comput. Methods Appl. Mech. Engrg*, **139**, 289–314, (1996).

[3] J.T. Oden, C.A.M. Duarte, O.C. Zienkiewicz. A new Cloud-Based Finite Element Method. *Comput. Methods Appl. Mech. Engrg*, **153**, 117–126, (1998).

[4] W.A.M. Brekelmans and J.H.P. de Vree. Reduction of mesh sensitivity in continuum damage mechanics. *Acta Mech.*, **110**, 49–56, (1995).

[5] Z. P. Bažant and G. Pijaudier-Cabot. Nonlocal dontinuum damage, localization instability and convergence. *J. Appl. Mech.*, **55**, 287–293, (1988).

[6] R.H.J. Peerlings and R. de Borst and W.A.M. Brekelmans and J.H.P. de Vree. Gradient Enhanced Damage for Quasi-Brittle Materials. *Int. J. Numer. Meth. Engng.*, **39**, 3391–3403, (1996).

Circumventing bifurcations in structural softening

J.G. Rots
Delft University of Technology, The Netherlands

S. Invernizzi
Politecnico di Torino, Italy

B. Belletti
Parma University, Italy, and Delft University of Technology, The Netherlands

M.A.N. Hendriks
Delft University of Technology, The Netherlands

Keywords: Softening, saw-tooth, bifurcation, sequentially linear, concrete, masonry, glass.

1 INTRODUCTION

In nonlinear finite element analysis the load is incremented in finite steps. Within these steps iterations are added to reach convergence. The use of finite steps implies that multiple integration points may crack simultaneously. Upon cracking, the local stiffness at these points switches from positive to negative following softening constitutive laws for quasi-brittle materials like concrete, masonry and glass. As a consequence of multiple softening points, the system of equations may become ill-conditioned, indicating loss of uniqueness, alternative equilibrium states or bifurcations of the equilibrium path. The issue for example occurs in perfectly symmetric specimens where left and right points crack simultaneously, or in reinforced concrete components where the reinforcement has a crack spreading tendency.

This paper rethinks the occurrence of bifurcations in a direct tensile test and in reinforced components of softening materials.

As an alternative to finite prescribed load increments, a scaled loading procedure is described in sequentially linear analysis with saw-tooth softening laws. This method allows only a single integration point to change status at a time, avoiding bifurcation problems.

2 RETHINKING A SYMMETRIC TENSILE TEST

At the end ‘80’s, the behavior of ‘direct’ tensile tests on notched plain concrete specimens was studied, experimentally by Hordijk (1991) and numerically by Rots (1988), Rots and De Borst (1989). Fig. 1 shows a result of a test. Up till peak the deformation is homogeneous. Near peak a strong non-symmetry occurs. The crack propagates from one side of the specimen, while the other side temporarily unloads. Depending on the boundary conditions, somewhere down the overall softening stress-displacement diagram the crack from the other side may be reloaded, rendering a homogeneous fully cracked state at complete softening.

Fig. 2 shows two numerical results, using a bilinear softening diagram as input. One result was achieved by modeling only half of the specimen, i.e. symmetric deformations were enforced. The other result was obtained by modeling the full specimen and perturbing the symmetry via an imperfection of 1 percent in the fracture energy G_f. The symmetric response shows an output stress-displacement diagram that fairly resembles the input bilinear diagram. Two cracks propagate simultaneously from two sides. The non-symmetric response shows a sharper peak at a slightly lower level, followed by a bump down the softening diagram. Here, the crack propagates from one side, while the other side unloads. The solution jumps to a lower and sharper non-symmetric equilibrium path. Later, the other side of the specimen is re-activated, giving a bump in the response. Finally, all integration points in the mid-section are softening and active

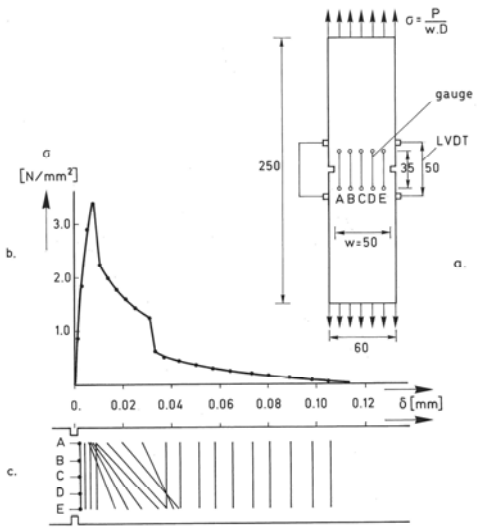

Fig.1. Experimental result of concrete direct tensile test (Hordijk 1991). (a) Specimen and instrumentation, (b) average stress-deformation curve over 35 mm gauge length, (c) distribution of deformations over the cross-section between the notches.

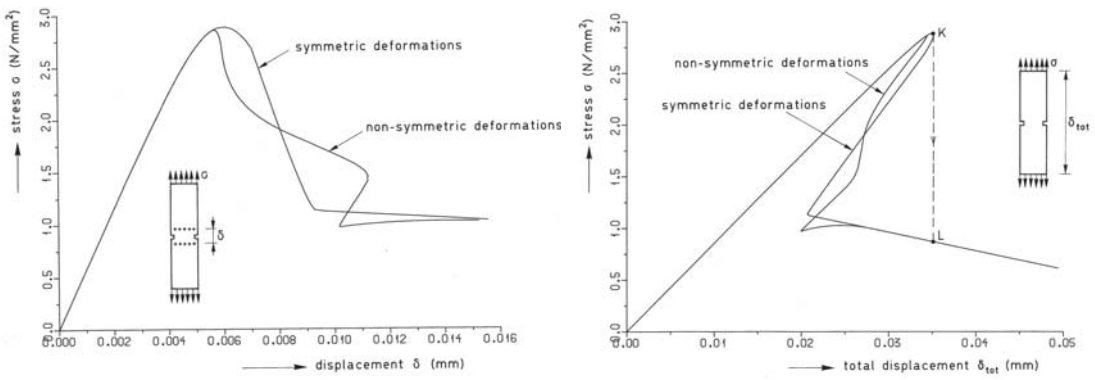

Fig.2. Computed stress versus average deformation, symmetry enforced and non-symmetry triggered (Rots 1988). Left: over gauge length 35 mm, right: over entire specimen length.

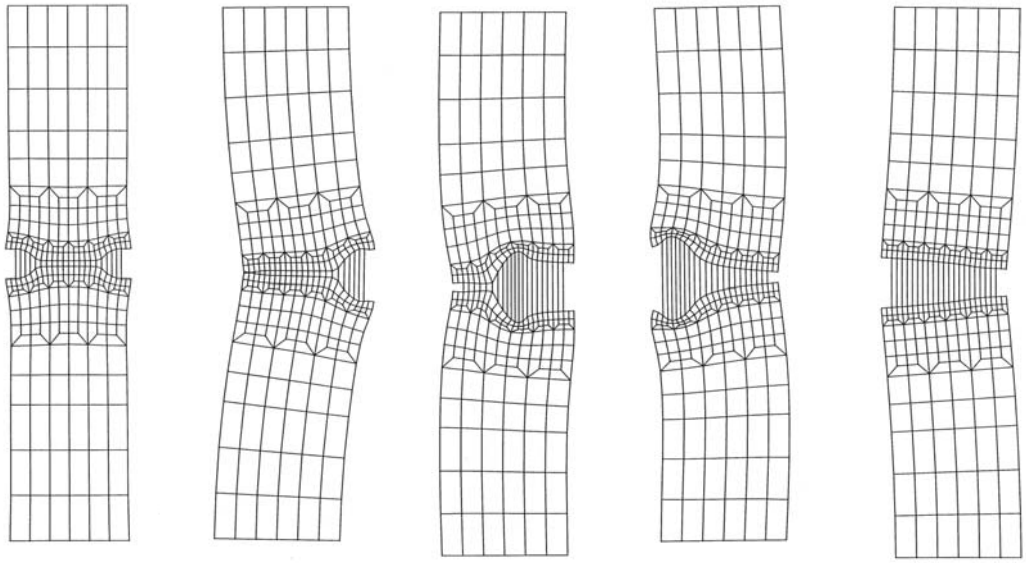

Fig.3. Computed incremental deformations, from left to right: pre-peak, at-peak, and three states post-peak (Rots 1988).

homogeneous deformation is achieved. Fig. 3 shows the deformation sequence. Numerically speaking, an unperturbed analysis of the full specimen gives a bifurcation point, with two post-bifurcation solutions: a symmetric one and a non-symmetric one. The direct solver then signals a singular system with two negative pivots and numerical instability occurs. The solution is to transfer the bifurcation point to a limit point. This can be done in two ways: first, by modeling only one half of the specimen and enforcing the symmetry, second, by modeling the full specimen and giving a material imperfection in combination with very small load or displacement increments triggering the non-symmetric mode. The actual physical response is always non-symmetric as nature is imperfect.

Rethinking this example, the conclusion is that alternative equilibrium states may occur and that an incremental-iterative approach can only trace the correct lowest equilibrium path when imperfections are added and the load steps are taken that small that there is no overshoot of the local material imperfection and/or a truly different stiffness at left and right side. In more complex cases, this requires a delicate interplay between adding representative imperfections and steering the analysis with very small steps, often in combination with arc-length techniques. Such interplay is not straightforward and poses demands to the analyst.

3 A SCALED SEQUENTIALLY LINEAR TECHNIQUE AVOIDING THE BIFURCATION

As an alternative to adding finite prescribed load increments, the bifurcation problem may be approached by a scaling procedure such that only one critical event, i.e. only one integration point status change from elastic to softening, occurs at a time. Then, non-symmetric modes are triggered automatically.

An example of such approach is a sequentially linear technique with saw-tooth softening (e.g. Rots and Invernizzi 2004, Rots, Invernizzi and Belletti 2006). Rather than a single nonlinear analysis, a series of linear analyses is performed keeping memory of local stiffness reduction. The softening curve of negative slope is replaced by a saw-tooth diagram of positive slopes. The incremental-iterative procedure is replaced by a scaled sequentially linear procedure, similar to procedures in some lattice models. Problems with negative stiffness and selection of loading/unloading statuses in multi-crack steps are avoided, as only one event takes places at a time. This model can be thought of as discretizing the space via finite elements, discretizing the local-softening via a saw-tooth diagram and re-computing the load via a scaling technique. Standard incremental-iterative Newton techniques rather discretize the space via finite elements, discretize the load via increments and re-compute the local softening on a continuous smooth diagram.

Using this model, a dog-bone specimen in direct tension was analyzed (Rots et al. 2006). The entire specimen was modeled, without imperfection. Due to the scaling procedure, always only one point is critical, and the non-symmetric mode occurs automatically. The stresses at left and right side will be the same or, more precisely, approximately the same. Due to computer accuracy, solver accuracy, node numbering, ordering of the system of equations the peak stress at the left side will always differ a fraction (e.g. 10^{-20} N/mm2) from the stress at the right side and only the highest stress is selected in the scaling procedure. That critical element will then jump into its next saw-tooth. In the next cycle, the linear analysis will detect that again the peak stress and thus critical point is at that side, and non-symmetry progresses. Fig. 4 shows the deformations and load versus displacement over the entire specimen length, indicating a snap-back that results from the series of linear analyses. As the boundary conditions in this test allowed free rotations, a bump as occurring for the Hordijk specimens with fixed boundaries did not occur. The conclusion is that the bifurcation is indeed circumvented by the scaling technique, triggering the non-symmetric mode automatically.

4 ALTERNATIVE EQUILIBRIUM STATES IN REINFORCED CONCRETE

Crisfield (1984) addressed the problem of alternative equilibrium states in reinforced concrete. Near the reinforcement, homogeneous tensile stress fields exist and multiple integration points may crack simultaneously in an increment of a nonlinear analysis. Here, not only two points

may crack simultaneously, but much more depending on step size versus mesh fineness and on the fact whether the bending moment distribution is constant or whether there is a gradient in it. Fig. 5 (left) shows a typical example of his results, indicating peaks and valleys, hard to trace, non-unique and heavily depending on solution procedures adopted. Fig. 5 (right) shows an example of a reinforced tensile bar analyzed with the sequentially linear technique, without imperfections. The alternative equilibrium states or multiple bifurcations are circumvented and a unique solution is achieved via the sequence of events, including local peaks, snap-backs and valleys, resembling the genesis of spaced primary cracks in RC practice.

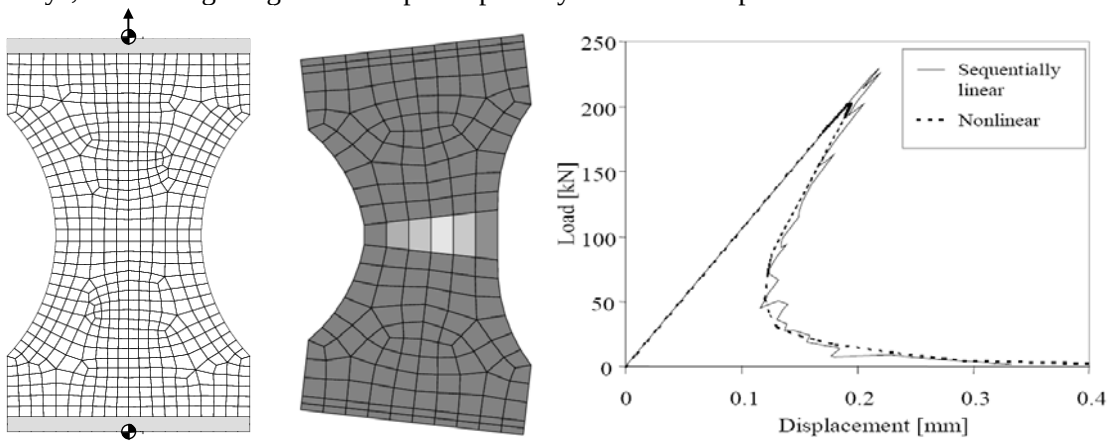

Fig.4. Mesh with boundary conditions, deformations beyond peak, and load-displacement response for sequentially linear analysis of dog-bone specimen.

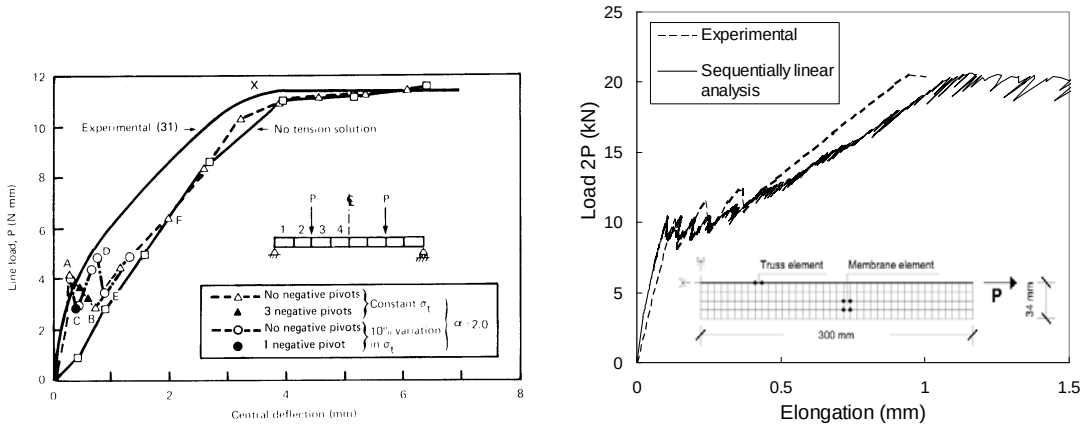

Fig.5. Typical numerical result for RC beam by Crisfield (1984) and for RC bar by sequentially linear saw-tooth softening model by Rots, Invernizzi and Belletti (2006).

REFERENCES

[1] Crisfield, M.A. (1984). Difficulties with current numerical models for reinforced-concrete and some tentative solutions. Proc. Int. Conf. Computer Aided Analysis and Design of Concrete Structures, Eds. F. Damjanic, N. Bicanic et al., Vol. I, 331-358.

[2] Hordijk, D.A. (1991). Local approach to fatigue of concrete. Dissertation, TU Delft, 210 pp.

[3] Rots, J.G. (1988). Computational modeling of concrete fracture. Dissertation, TU Delft, 132 pp.

[4] Rots, J.G. and De Borst, R. (1989). Analysis of concrete fracture in direct tension. Int. J. of Solids and Structures, Vol. 25, Issue 12, 1381-1394.

[5] Rots, J.G. and Invernizzi, S. (2004). Regularized sequentially linear saw-tooth softening model. Int. J. Numer. Anal. Methods Geomechanics, Vol. 28, 821-856.

[6] Rots, J.G., Invernizzi S. and Belletti, B. (2006). Saw-tooth softening/stiffening – a stable computational procedure for RC structures. Computers and Concrete Vol. 3, No. 4, 213-234.

Finite element analyses help develop a diagnostic aid for masonry

I.A.E. de Vent, J.G. Rots & G.J. Hobbelman
Faculty of Architecture, Delft University of Technology, Delft, the Netherlands

Keywords: diagnosis, structural damage, masonry, nonlinear finite element analysis

1 INTRODUCTION

Both in medicine and in building pathology, the quality of the initial hypothesis is crucial for an efficient diagnostic process. In general, this initial hypothesis is based on a visual inspection of the symptoms of damage, taking into account the material, geometrical, and environmental context. However, a major problem when dealing with structural damage is that these symptoms and context conditions are usually not interpreted explicitly. As a result, the diagnostic process may be confronted with an incomplete, if not irrelevant, hypothesis. Apart from the fact that this delays the diagnostic process, it may also result in higher costs for testing.

To allow for a more efficient and successful diagnostic process, a research project has been started that systematically investigates how symptoms and context of structural damage in masonry can be related to specific damage processes. It intends to propose an objective guideline for the interpretation of these signs, explicating those conditions that are essential and sufficient for distinguishing between damage processes.

As part of this research project, finite element analyses are used to study the relation between settlement troughs and damage symptoms. We analysed two models (one wall with openings, one without) under four displacements imposed on their bases. The results provide insight into the influence that location and relative size of a settlement trough have on the eventual damage pattern. In this way, we have been able to confirm and define damage characteristics that can be specifically linked to certain settlement profiles.

2 OUTLINE OF THE FINITE ELEMENT ANALYSES

2.1 *Geometry, mesh, and constraints*

Object of the current study is the sidewall of an average Dutch church building. We modelled two variants: one blind wall, and one with openings. Both 2D models consist of a wall of eight bays, each 4.80 m wide and 10.00 m high, with a thickness of 785 mm. Below the wall, a strip of 1.20 m high and 1027 mm thick represents a stepped foundation.

The elevations were meshed with plane stress elements: 400 x 400 mm eight-node curved quadrilateral CQ16M elements for all orthogonal parts, and six-node curved triangular CT12M elements for the irregular wall areas next to the windows. Below the foundation we modelled an interface, represented by three-plus-three-node curved line CL12I structural interface elements.

To support the wall, translations along the y axis have been suppressed for all nodes at the lower boundary of this interface, while the right end node of this edge has also been constrained for translations along the x axis. The geometries, meshes, and constraints are shown in Figure 1.

2.2 *Material models for masonry and no-tension interface*

As we are primarily interested in the global structural behaviour, we have modelled the masonry of wall and foundations with homogeneous, isotropic properties. A smeared total strain rotating crack concept was applied to represent the brittle failure behaviour of masonry. This crack concept is characterised by a crack orientation that is continuously updated with the direction of the major principal stresses [Rots 1988]. It is robust and does not require the input of predefined crack paths, thus allowing us to study where and in which directions cracks occur.

Consistent with the study of Hendriks et al. [1995], we assumed the following material properties for the brick masonry: Young's modulus $E = 6000$ N/mm^2; Poisson's ratio $v = 0.2$; tensile strength $f_t = 0.30$ N/mm^2; compressive strength $f_c = 8$ N/mm^2; mode-I tensile fracture energy $G^I_f = 0.05$ N.mm/mm^2; and density $\rho = 2.0.10^{-6}$ kg/mm^3. The tensile behaviour of the masonry has been described with a linear tension softening curve, while a constant, ideal relation between stress and strain was chosen for compression, see Figure 2.

Since we intend to investigate the behaviour of the wall and not that of the ground, we opted for a semi-coupled model [Boonpichetvong and Rots 2004], in which a no-tension interface reproduces the bond between building and soil: stiff under compression, and weak under tension. Following an approach similar to the one used by Rots [2000], we calculated a representative spring stiffness for a 2.80 m high 'beam' of fairly compact sand. This led us to a value of 0.030 N/mm^3 for the normal stiffness k_n in compression. The transfer of tensile stresses was prevented by setting the stiffness in tension at 3.10^{-8} N/mm^3, while the influence of horizontal ground movement on the building was eliminated by assuming an almost zero value for the tangential interface stiffness $k_t = 1.10^{-15}$ N/mm^3. The interface properties are schematised in Figure 3.

2.3 *Loads*

Three loads were imposed on the models: a gravity load, a line load, and a displacement load. The gravity load was derived from the models' geometry and mass density, while a line load of 11.0 N/mm was applied on the top edge of the wall to reproduce the weight of a wooden ceiling and a tiled wooden roof. Settlement was simulated by four vertical displacement curves, each with a maximum vertical settlement of 100 mm, imposed on the lower edge of the interface.

An incremental-iterative solution procedure was adopted. First, the gravity load and the line load had been activated, after which all resulting displacements were suppressed. Then, the displacement load was imposed incrementally. As each increment corresponds with a percentage of the total displacement, the shape of the trough stayed constant throughout the analysis.

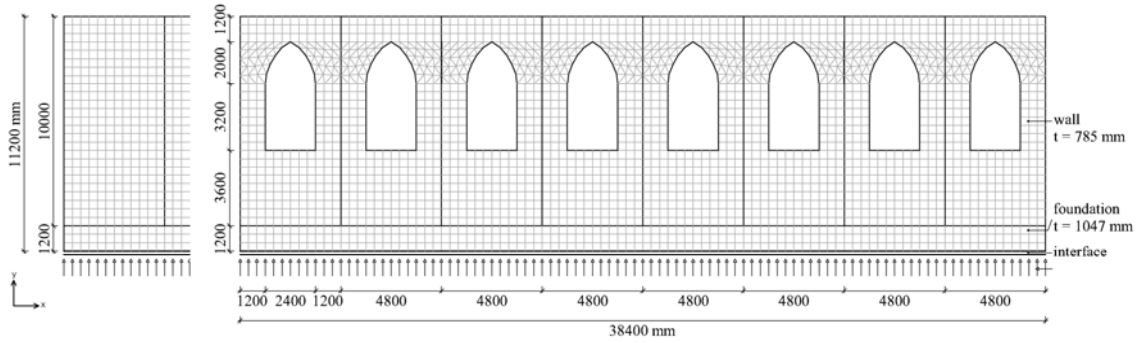

Figure 1: Meshes of part of the blind wall (l) and of the wall with openings (r), with dimensions indicated.

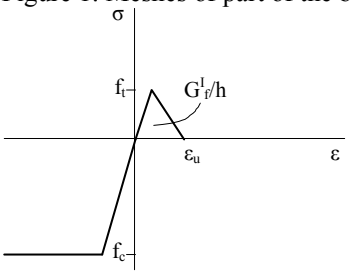

Figure 2: Masonry model.

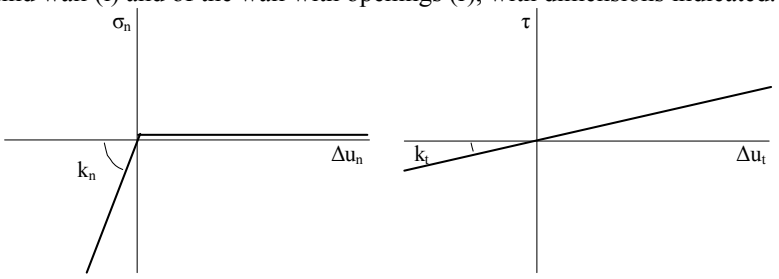

Figure 3: Interface behaviour in normal (l) and tangential (r) direction.

3 RESULTS

Eight load-model combinations have been tested. Figure 4 summarises the results for each of these combinations, most importantly the deformations of wall and foundation compared to the imposed vertical displacements; and the development of partial and full cracks.

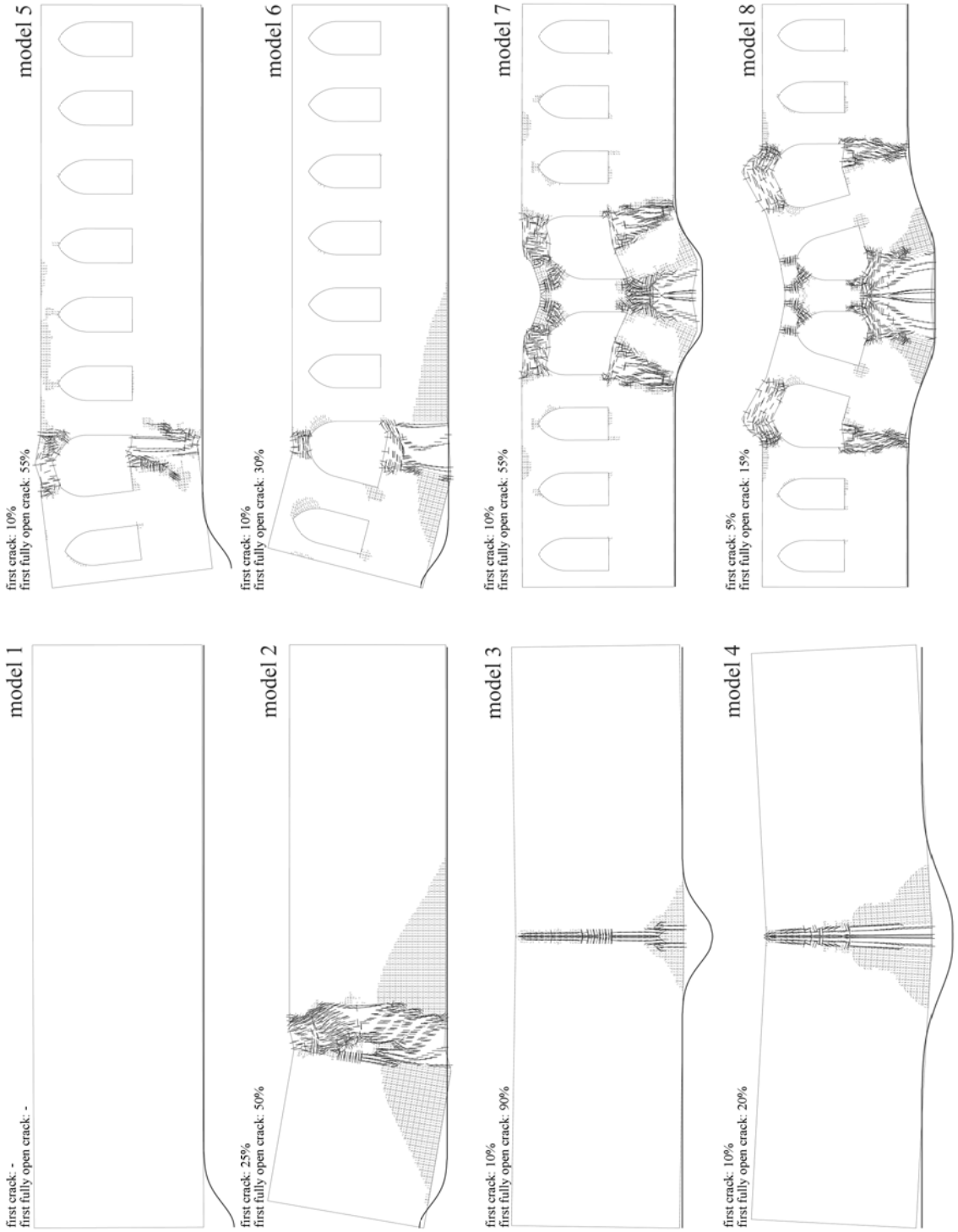

Figure 4: Deformations and cracks for the eight load-model combinations. The bold lines at the bottom indicate the full (100%) imposed vertical displacement; the occurrence of cracks is expressed in a percentage of this full displacement load. The strong lines within wall and foundation represent fully open cracks, while the thinner lines are partial (hair) cracks. Deformations have been scaled 20 times.

4 DISCUSSION

The eight load-model combinations allowed us to study the influence that wall openings and type, location, and relative size of a settlement trough have on damage characteristics.

By comparing the results for the walls without (models 1-4) and with openings (5-8), the expectation was confirmed that walls with openings are more vulnerable to settlement: cracks occurred earlier, were sooner fully open, and showed larger displacements. Also, it was demonstrated that the final damage pattern is strongly influenced by the presence and position of openings. While all matching models show a comparable overall behaviour at the start, in the blind walls all damage remains concentrated in one vertical crack, while for the walls with openings this vertical crack snaps towards a window. Especially for mid-settlements (7, 8), the windows gave rise to a series of cracks that divided the wall in separate parts, helping it to adjust to the trough and recover its support.

The end-settlement (1, 5) and its opposite, end-heave (2, 6), both result in a vertical crack along the full height of the wall. The development and rotation are, however, opposite: Under end-settlement, cracking starts at the top of the wall, with a resulting crack that is widest at the top; while for end-heave, the crack starts at the bottom and is widest at the bottom.

Comparing the models 1, 2, 5, and 6 to models 3, 4, 7, and 8, it becomes clear that mid-settlements lead to cracks directly above and symmetric to this settlement, while for end-settlements (or heaves) cracks develop at some distance of the displacement. In the latter case, the actual position of the damage appears to be more influenced by local weaknesses such as openings, than by the trough itself.

Finally, the results for the mid-settlements of different trough lengths (3, 4, 7, 8) indicate that this length does influence the extent of the damage. Longer troughs lead to larger areas where cracking occurs, especially when there are openings in the wall, and to larger displacements and rotations. Although the cracking starts almost at the same percentage of displacement, fully open cracks occur much earlier. Nevertheless, the resulting damage patterns are quite similar.

5 CONCLUSIONS

The use of FEA made it possible to study the behaviour of walls with and without openings under four displacement curves. The main conclusion is that the actual damage pattern is strongly influenced by local imperfections or weaknesses in a structure. The presence of such weak points should, hence, explicitly be taken into account in an on-site survey.

For the interpretation of cracks in relation to settlement, we can state that changes in crack width along the crack length indicate the point, but not the direction of rotation. Hence, a crack that is widest at the bottom can be related to settlement below this crack, or heave at one or both sides; and a crack that is widest at the top can result from settlement at one or both sides, or from heave below this crack. Here, deviations from the horizontal of bed joints can help indicate at which side displacements have occurred, and where the cause should be searched for.

As a follow-up to this study, a physical zero-tension model is now tested: separate blocks cut out of medium-density fibreboard. With this mdf model, the influence of weak mortar joints will become clearer, and we expect to see more diagonal shear cracks. In addition, this model will allow us to truly test the walls on their in-plane stability. While stability has been no issue in this FEA study, it is in fact the most important criterion for failure in masonry [Heyman 1995].

REFERENCES

Boonpichetvong, M., and Rots, J.G. (2004). "Settlement damage of masonry buildings in soft-ground tunnelling." The Structural Engineer, 83(1), 32-37.

Hendriks, M.A.N., Rots, J.G., and van Staalduinen, P.C. (1995). "Onderzoek naar te verwachten zettingschade bij aanleg van de noord/zuidlijn in Amsterdam." 95-CON-R0343, TNO Bouw.

Heyman, J. (1995). The stone skeleton; Structural engineering of masonry architecture, Cambridge University Press, Cambridge.

Rots, J.G. (1988). Computational modeling of concrete fracture, Technische Universiteit Delft, Delft.

Rots, J.G. (2000). "Settlement damage predictions for masonry." Maintenance and restrengthening of materials and structures: Brick and brickwork. Proc. Int. Workshop on urban heritage and building maintenance, 47-62.

TNO DIANA BV. (2008). "iDIANA Release 9.3." Delft.

Modeling of long-term deformations and damage accumulation in masonry

E. Verstrynge & L. Schueremans
Department of Civil Engineering, KULeuven, Kasteelpark Arenberg 40, 3001 Heverlee, Belgium; e-mail: els.verstrynge@bwk.kuleuven.be

M.A.N. Hendriks
Faculty of Civil Engineering and Geosciences, Delft University of Technology, the Netherlands

Keywords: masonry, damage accumulation, creep modeling, experimental research

1 INTRODUCTION

High, sustained loads in masonry cause time-dependent deformations, which can lead to failure of the construction. This phenomenon mostly occurs in high constructions, such as historical towers, where the dead load imposes significant stresses on the base of the tower [4]. As knowledge and experimental data are lacking to describe this time-dependent behavior in historical masonry, a research program has been set up [1]. Aim of the research described in this paper is to obtain a structural model and parameter values in order to predict creep failure in masonry. A rather extensive series of accelerated creep tests is performed in order to obtain an average value and standard deviation for the model parameters. The long-term behavior is simulated with these parameter values and the model predictions are validated with the results of long-term creep tests.

2 PARAMETER CALCULATION FROM EXPERIMENTAL RESEARCH

For the experimental research, 36 masonry columns with dimensions 19*19*60 cm (l*b*h) were constructed at the laboratory Reyntjens (Fig 1). The columns were composed of 10 brick layers, with two bricks per layer and a mortar thickness of 1 cm. An air-hardening lime mortar was used, in a composition which is representative for historical masonry.

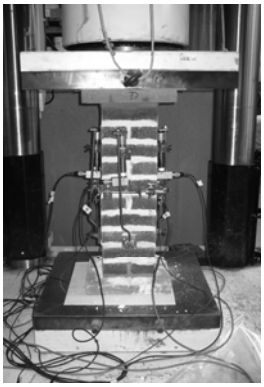

Fig 1. Test set-up

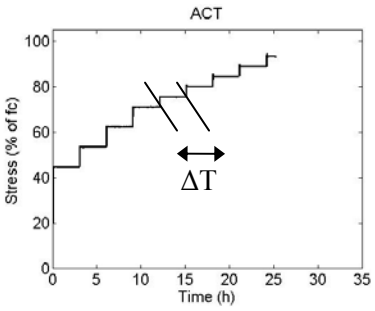

Fig 2. Loading path followed during ACT

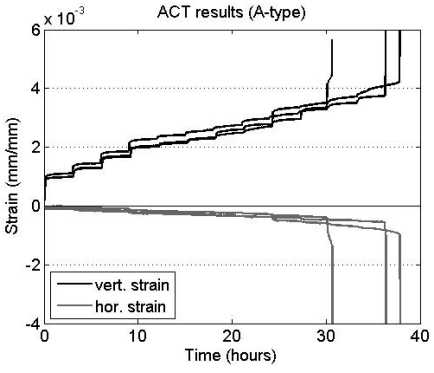

Fig 3. Results of strain evolution during ACT on 3 specimens

Different types of tests were performed to gather knowledge on the masonry's time-dependent behavior. The types of tests, important for the model described below, are listed:

- Monotonic compressive tests: to obtain short-term strength parameters (compressive strength, Young's modulus) to calculate the load path for the creep tests (see Fig 2)
- Short-term or accelerated creep tests (ACT): to calculate the parameter values for the creep modeling. The time interval for each step $\Delta T = 3$ hours. Each step of the test indicates a primary creep phase (decreasing strain rate), a secondary creep phase (constant strain rate, with a slope which depends on the stress level) and in the last step, a tertiary creep phase (increasing strain rate) before failure occurs. The parameters are calculated from these different phases, as the model is based on a phenomenological approach.
- Long-term creep tests: these tests are still partly ongoing as they have a duration of two years ($\Delta T = 2$ months). The results are used to validate the model predictions.

3 RHEOLOGICAL MODEL

The visco-elastic model used to describe the time-dependent deformations consists of a Maxwell and a Kelvin model in series, as presented in Fig 4. This configuration is often used to describe creep effects [2, 3] as it is able to capture the first two phases of a typical creep curve.

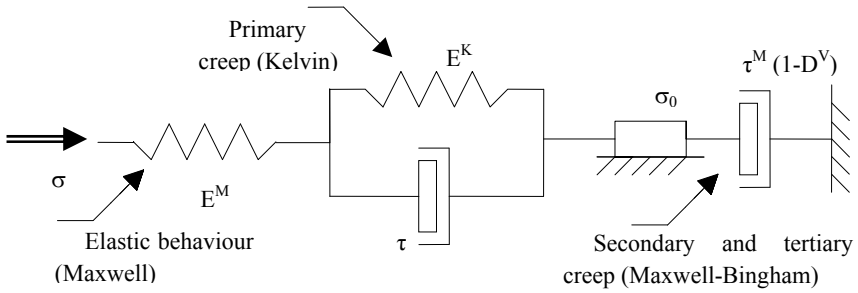

Fig 4. Schematic 1-dimensional presentation of rheological model

Furthermore, a damage parameter /D^V/ is added to the model in order to describe the damage accumulation and loss of material cohesion, which will trigger the unstable strain increase of the tertiary creep phase and lead to failure of the masonry.

The behavior of the Maxwell-Kelvin chain can be described as a second order differential equation. If a constant stress is applied at t = 0 and all model variables remain constant in time, this differential equation can be integrated in a closed-form 1-dimensional constitutive equation:

$$\varepsilon(\sigma,t) = \frac{\sigma}{E^M} + \frac{1}{E^K}\left(1 - \exp\left(\frac{-t}{\tau^K}\right)\right)\sigma + \frac{t}{E^M \tau^M \left(1 - D^V\right)}\sigma \tag{1}$$

/$E^{M/K}$/ is the Maxwell (M) or Kelvin (K) elastic modulus and /$\tau^{M/K}$/ the Maxwell (M) or Kelvin (K) time constant. /D^V/ is the viscous damage parameter, which increases from 0 (no damage) to 1 (failure). Experimental research has indicated that the evolution of /D^V/ has a dual formulation; it increases linearly in function of the stress level to describe the dependency of the slope of the secondary creep phase on the stress (equation 2) and it follows a damage rate formulation in function of time to describe the tertiary creep phase (equation 3):

$$D^V = A\sigma^* + B \tag{2}$$

$$\dot{D}^V = c\left(\frac{\sigma^*}{1 - D^V}\right)^n \tag{3}$$

With /σ*/ the dimensionless stress ratio, calculated by dividing the stress by the average compressive strength, obtained from the compressive tests. When other stress paths and non-

constant model variables are considered, the integration is approximated with an incremental formulation:

$$\Delta\varepsilon_i = \frac{\Delta\sigma_i}{E_i} + \Delta\varepsilon_i^{in} \tag{4}$$

This formulation was implemented in Matlab (The MathWorks, version 2008a). Fig 5 indicates simulations made with the 1-dimensional model. The simulation (black line) represents the experimental results rather well. The small dotted lines indicate simulations made with the 5% upper and lower quantile values of the compressive strength /f_c/ and the Maxwell Young's modulus /E^M/. Most experimental strain values are within these boundaries. Fig 6 presents a simulation of the long-term creep tests, using the average parameter values obtained from the short-term creep tests. As expected, the experimental results show a larger scatter (grey lines), but again the simulation predicts the experimental behavior rather well. Two specimens have already failed within the 5% boundaries, the tests on a third specimen are still ongoing.

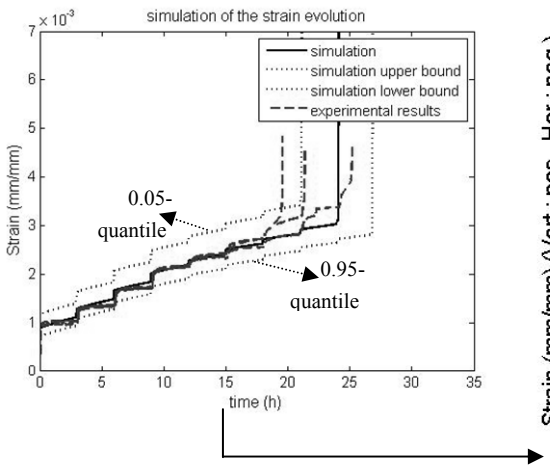

Fig 5. Simulation of short-term creep tests and experimental results

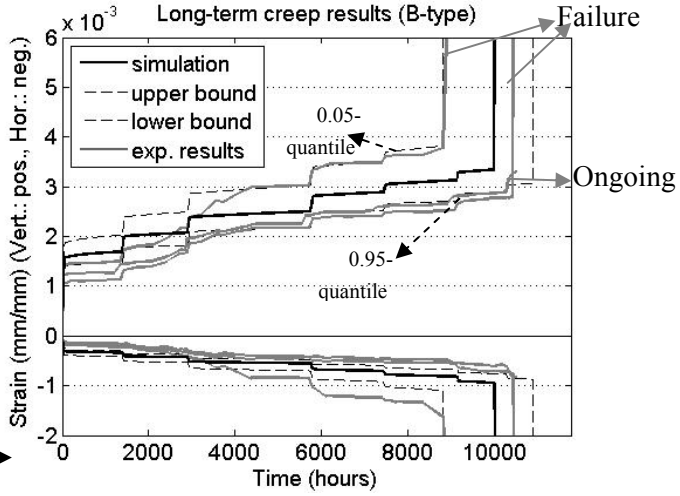

Fig 6. Simulation of long-term creep tests and experimental results

4 THREE-DIMENSIONAL ISOTROPIC MODEL WITH ORTHOGONAL DAMAGE EVOLUTION

In order to make a more accurate simulation of the damage accumulation in historical masonry towers, an attempt is made to implement the rheological model in a finite element code. A three-dimensional version of the model is implemented in DIANA, using the User Supplied Subroutine 'USRMAT', in which a general user defined structural model can be implemented. As the model is implemented in a strain-driven form, equation 4 is inverted into a pseudo-elastic formulation:

$$\Delta\boldsymbol{\sigma}_i = \boldsymbol{C}_i^{-1}\left(\Delta\boldsymbol{\varepsilon}_i - \Delta\boldsymbol{\varepsilon}_i^{in}\right) \tag{5}$$

With /$\mathbf{C}_i$/ being the compliance matrix at time $t = t_i$. The model is isotropic until damage occurs, thereafter, orthotropic material behavior is described by damage growth in three orthogonal directions. The damage evolution in one direction can be modeled to depend on the principal stress components. In this manner, dilatation effects and restrained damage growth due to lateral confining stresses can be simulated, as presented in Fig 7 (simulations made with $\Delta t = 120$ sec).

These initial analyses were made on small rectangular test specimens, consisting of 20-node solid brick elements. For implementation of the model to be used for more complex structures and analysis, including stress redistributions, a more detailed model will be elaborated. Therefore, rotation of the damage direction towards the principal strain axis and a more consistent tangent will be formulated.

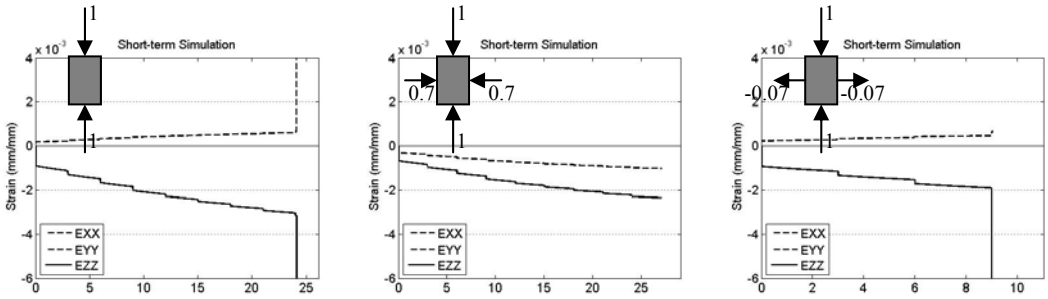

Fig 7. Axial and lateral strain evolution during a simulation of an accelerated creep test. The strain values and moment of failure depend on the size and direction of the lateral confining stresses.

Fig 8 indicates the initial axial and lateral stresses and damage under dead load of a simplified brickwork tower (dimensions 5*5*30 m) at time t = 0. In order to clearly see the damage pattern, the weight of the tower has been multiplied by four. Vertical compressive stresses and damage are present at the base of the tower and around the lower window. Lateral tensile stress and damage occurs above and below the windows as expected. In order to extend this analysis in time, the model will be adjusted according to the necessary modifications indicated above.

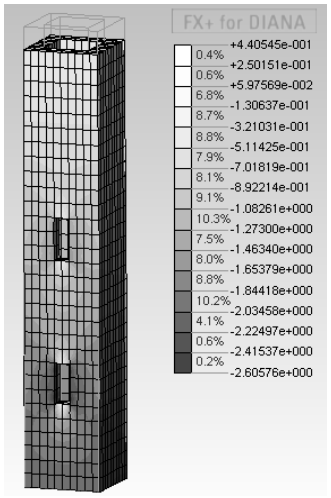

Fig 8a. Axial stresses

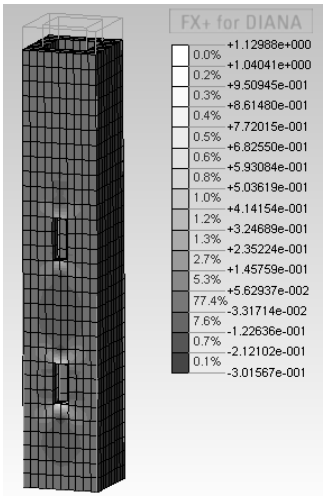

Fig 8b. Lateral stresses

Fig 8c. Axial damage

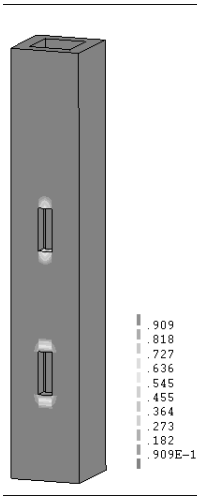

Fig 8d. Lateral damage

Fig 8 a-b shows the coarseness of the solid element mesh. This simplification could lead to inaccuracies, particularly around the window openings, but a smaller mesh will increase the necessary calculation effort too much. A locally refined mesh or the use of shell elements could be a solution. The chosen macro-modeling approach will not be able to represent all complex phenomena which occur, such as the brick-mortar interactions, but already needs a long calculation time within the time-dependent framework and appears therefore to be a practical starting point for the presented study.

5 REFERENCES

1. Binda, L., et al., Long term compressive testing of masonry - test procedure and practical experience, in 6th International Seminar on Structural Analysis of Historical Constructions, D. D'Ayala and E. Fodde, Editors. 2008: Bath. p. 1345-1355
2. Boukharov, G.N., M.W. Chanda, and N.G. Boukharov, The three Processes of Brittle Crystalline Rock Creep. International Journal of Rock Mechanics and Mining Sciences and Geomechanics Abstracts, 1995. **32**(4): p. 325-335.
3. Papa, E. and A. Taliercio, A visco-damage model for brittle materials under monotonic and sustained stresses. International Journal for Numerical and Analytical Methods in Geomechanics, 2005. **29**(3): p. 287-310.
4. Verstrynge, E., et al., Application of the acoustic emission technique for assessment of damage-accumulation in masonry. International Journal for Restoration of Buildings and Monuments, 2008. **14**(3): p. 167-178.
5. Verstrynge, E., L. Schueremans, and D. van Gemert, Life time expectancy of historical masonry structures subjected to creep - a probabilistic approach, in 6th International Probabilistic Workshop, C.A. Graubner, H. Schmidt, and D. Proske, Editors. 2008: Darmstadt. p. 247-260.
6. Verstrynge, E., L. Schueremans, and D. van Gemert, Service life prediction of masonry under high loading: modelling and probabilistic evaluation, in 10th International Conference on Structural Safety and Reliability. 2009: Osaka.